Integrated Infrared Sensor Platform

by
Zhaohong Han
B.E., Materials Science and Engineering
Tsinghua University, China, 2011

Submitted to the Department of Materials Science and Engineering in partial fulfillment of the requirements for the degree of

DOCTOR OF PHILOSOPHY IN MATERIALS SCIENCE AND ENGINEERING AT THE MASSACHUSETTS INSTITUTE OF TECHNOLOGY

February 2017

Signature of Author: Signature redacted
Department of Materials Science and Engineering
September 8th, 2016

Certified by: Signature redacted
Lionel C. Kimerling
Thomas Lord Professor of Materials Science and Engineering
Thesis Supervisor

Certified by: Signature redacted
Anuradha M. Agarwal
Principal Research Scientist, Materials Processing Center
Thesis Supervisor

Certified by: Signature redacted
Jurgen Michel
Senior Research Scientis, Materials Processing Center
Thesis Supervisor

Signature redacted

Accepted by:
Donald Sadoway
Professor of Materials Science and Engineering
Chair, Departmental Committee on Graduate Student

Integrated Infrared Sensor Platform

by

Zhaohong Han

Submitted to the Department of Materials Science and Engineering on September 8th , 2016 in Partial Fulfillment of the Requirements for the Degree of Doctor of Philosophy in Materials Science and Engineering

Abstract

Infrared spectrum, especially mid-infrared range (2.5~12μm) covers the absorption peaks of many important chemicals including carbon monoxide, methane and water vapor. By analyzing the absorption spectrum of achemical, one can measure the concentration of the chemicals as well as distinguish the chemical species. The purpose of this work is to build a Si CMOS compatible integrated mid-infrared (MIR) platform for sensing.

In this work, we evaluated the three major components (materials and devices) comprising an integrated mid-infrared (MIR) sensing platform: the light source, the waveguide sensor and the detector.

To build an integrated MIR light source, we evaluated three approaches. 1) Germanium light source, which is the representative of the CMOS compatible semiconductor light source. By applying tensile strain as well as increasing doping and injection level, Ge is tuned to pseudo-direct or direct bandgap structure and the emission wavelength extends to MIR range. 2) Er-doped GaLaS (GLS) platform which is the representative of the rare earth doped material system. A new laser structure is designed

for this system with a threshold power of 7.6 μW and a slope efficiency of 10.26%. 3) Frequency comb generation which is a new area using nonlinearity to generate new frequencies. Thick Si_3N_4 material for comb structures are designed, fabricated and tested.

In the waveguide sensor section, a waveguide structure based on chalcogenide glass (ChG) is built and tested. The sensing limit for methane reaches 2.5 vol. %. Besides, a ChG based small-footprint plasmonic optical switch is designed to work as an optical router for integrated spectrometer applications with a small (167 nm long) footprint.

In the last part, a MIR PbTe based integrated detector has been successfully demonstrated for the first time. A further improvement in the material property and device structure yields a responsivity is about 1.4 A/W in the MIR regime.

Thesis Supervisors:

Lionel C. Kimerling

Title: Thomas Lord Professor of Materials Science and Engineering

Anuradha M. Agarwal

Title: Principal Research Scientist, Materials Processing Center

Jurgen Michel

Title: Senior Research Scientist, Materials Processing Center

Acknowledgements

I want to express my deepest appreciation to those who have accompanied me during my work and life at MIT.

First and foremost, I would like to thank my advisors, Professor L. C. Kimerling, Dr. Anuradha Agarwal and Dr. Jurgen Michel, for their tireless efforts in nurturing me into an independent researcher and ceaseless support for my professional and personal development. It was through their limitless passion and rigorous training that this thesis and my Ph.D. career at MIT have been made possible.

I would like to thank Professor Polina Anikeeva and Professor Caroline Ross, who have given me great support and advice as my committee members. Many of my colleagues and collaborators have helped me greatly to complete this work. I feel lucky to have spent my five years in the EMAT group, which is like a family. The "parents", my advisors, provided suggestions in both academic and daily life. The "elder brothers", Prof. Juejun Hu and Prof. Jifeng Liu, are my teachers and friends. I would especially like to thank Dr. Vivek Singh, Dr. Yan Cai, Dr. Rodolfo Camacho-Aguilera, Dr. Lin Zhang, Dr. Jianwei Mu and all other "ematters" who were working with me together. It was my great pleasure to work with you and learn from you. And my "twin brother and sister", Corentin and Wei, I will never forget the time we studied, worked and played together. Every time I needed someone to talk to, you were always sitting next to me with smiles on your faces. And last but not the least, our "neighbors", the PMAT students, you made my life more colorful. Qingyang, Derek, Hongtao and Lan, thanks for your support in my experiments and designs!

Finally, I want to give my deepest thanks to my family, especially my parents and my dear twin brother, for their wholehearted support and love. For my best friend, collaborator, roommate, twin brother, Dr. Binghong Han, thanks for all your help in my life.

Table of Contents

List of Figures

List of Tables

Chapter 1. Introduction

1.1. Motivation

Photonic devices are widely used in different areas including communication, personal electronics and environment monitoring. During the last decades, photonic components including light sources and photo detectors have been developed to cover a wide range of wavelengths from the ultraviolet to the infrared. These components are not only faster and more accurate, but also smaller so that we can integrate them onto a chip. Integration of photonic devices not only shrinks the footprint of the device, but also decreases the fabrication cost and increases its stability against electromagnetic interference.

Nowadays an increasing number of applications in the industrial sectors as well as in daily life require different kinds of sensors. The functions cover sensing gravity, speed and acceleration, light, fingerprint reading to detecting special chemicals. Today one smartphone usually contains more than 10 sensors. The integration of photonic devices makes it possible to put optical sensors into our mobile devices or build distributed sensor networks.

Among all these applications, chemical vapor sensing is one of the most important functions of the optical sensor. For example, with the help of these sensors, one can quickly obtain air pollution conditions around them and figure out if the current situation is good for jogging. Or with a portable toxic gas detector, one can be warned when there is CO or other dangerous gases around so as to avert tragedies. Integrated photonics plays

an important role in on-chip chemical sensing. Changes in the real and imaginary parts of the complex refractive index can be used to rapidly detect the presence of chemical species with high sensitivity. In particular, the mid-IR wave band (2.5 to 12 μm) represents a strategically important spectral regime for photonic sensing applications, as characteristic absorption fingerprints of most molecules reside here. The absorption spectra of several chemicals are shown in Figure 1-1. The MIR spectra analysis can provide accurate quantity as well as selective measurement of chemical vapors.

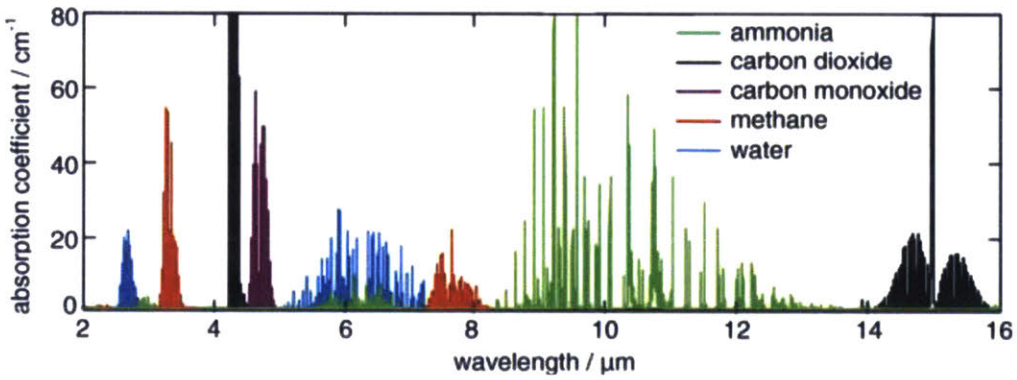

Figure 1-1 The absorption spectrum of chemical vapors in MIR range[1].

Current MIR spectrum analysis uses large equipment, such as Fourier transform infrared spectroscopy (FTIR). The tools are expensive and inconvenient. People have to bring samples back to the lab for measurements. Integrating the whole sensing platform onto a chip ("lab-on-chip") can solve this problem. It shrinks the size of the tool to pocket-size which people can do on-site measurement. The benefit of large volume production can decrease the price. Integration with other CMOS technology, including computing, remote communication, power management, etc. makes the sensing platform "smart" and be able to monitor the chemical vapor individually and remotely.

1.2. Integrated MIR Sensor Platform

To build a lab-on-chip sensing platform, one needs an optimized planar solution for each part, including a light source, a waveguide sensor and a detector.

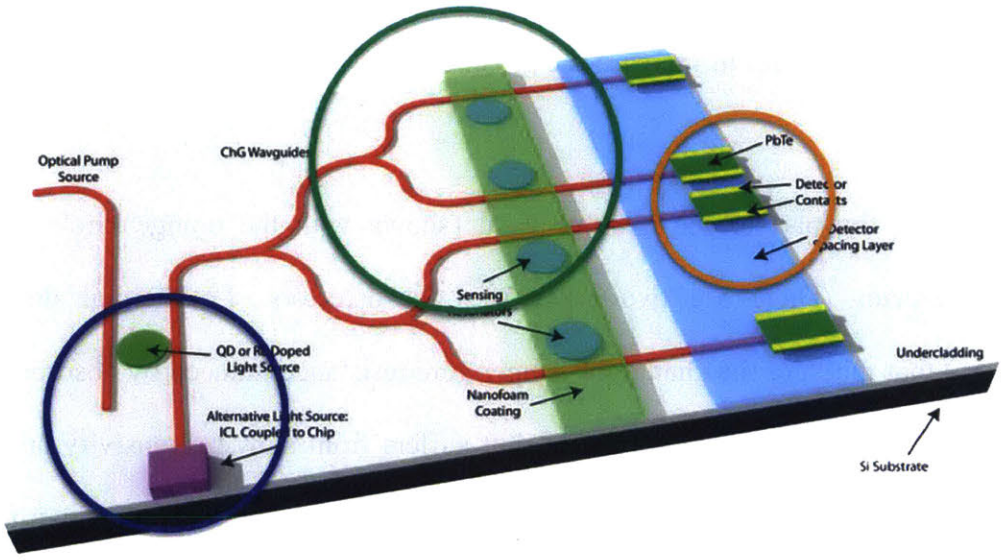

Figure 1-2 A schematic of our MIR gas sensing platform[2].

A schematic of the integrated MIR sensing platform is shown in Figure 1-2. On the left side is the light source (in blue circle) which shows optically-pumped quantum dots (QD) or a rare earth (RE) doped light source using a disk-resonator. Similar structures can also be used for frequency comb generation. Pump light (visible or near infrared) is delivered into the resonator, interacts with active material and generates new wavelengths in the MIR range. Other than the optically driven light source, quantum cascade laser (QCL) or interband cascade laser (ICL) [3-6], although expensive, are also alternative MIR source with fine linewidth and wide tuning range. Extra wafer bonding and alignment are needed for these latter light sources.

The middle section comprises waveguide sensors (in green circle) which can be resonators to increase the interaction distance between vapor and light, sacrificing the broadband character (detecting resonant wavelengths only), or a plain waveguide without a resonator structure in which one is able to increase light interaction with analytes by introducing spirals or paper-clip structures. The surface can be modified by other chemicals such as polymers to increase the sensitivity as well as the selectivity of certain vapors[7].

In Fig 1-2, the part to the extreme right (shown with the orange circle) is the integrated detector. There are two types of light detectors. 1) Thermal detectors (bolometers) that measure the change of temperature/resistance induced by absorption of photons. This kind of detector is low-cost, but suffers from slow responsivity and low sensitivity[8]; 2) A photonic detector which relies on carrier generation induced by infrared photons offers better speed and sensitivity than a thermal detector, and is selected in our system.

Spectral analysis can be accomplished in two ways. 1) We can change the light emission wavelength of the source and scan the entire spectrum. Semiconductor or rare earth doped light sources allow wavelength tuning by changing the cavity resonance peaks, which is usually accomplished by tuning the temperature[9] or mechanically changing the cavity structure[10]. The tuning range is limited by the gain spectrum of the active material; 2) We send broadband light (pulsed laser or frequency comb) to the sensor and analyze the output spectra by splitting the light according to its wavelength (for example, using grating structures). For single-detector structures, optical routers and switches (spectrometers) are needed to control the light path. For multi-detector

structures, the output spectrum is analyzed by parallel detection of each channel, one for each set of wavelengths.

1.3. Integrated MIR Light Source

Integrated light source for communication wavelength is widely studied due to its industrial potential, especially Germanium laser and III-V hybrid laser with wafer bonding technology [9,11,12]. But when pushed to mid-IR, the choices become narrower. QCL or ICL give fine tuning range and linewidth, but are expensive and unsuitable for mass production because their fabrication is not CMOS-compatible. In our study, three different options for on-chip mid-IR light sources are considered as future candidates.

Intrinsic Germanium has a bandgap of 0.8 eV, which is 1550 nm. However, to make it a direct-bandgap material, strain is applied which shrinks the bandgap. High doping level also helps making it a "pseudo-direct bandgap", which can further decrease the emission wavelength due to band gap narrowing effect. For example, with 2% tensile strain, Germanium becomes a direct bandgap material with bandgap of 0.5 eV (2480 nm)[13]. **Chapter 2** introduces the band engineering study of Ge and its band gap narrowing effect. Quantum effects on Ge light source are also discussed.

The second candidate is a rare-earth doped material system where the emission wavelength is locked by atomic energy levels. Er^{3+} ion, for example, has a transition of 3.6 μm when pumped by 660 nm red light. However, such transitions face low quantum efficiency and short lifetime issues, requiring high-Q cavity for both pump and signal wavelengths, which have almost five times difference in wavelength (660 nm vs 3600 nm). **Chapter 3** presents a feasible design for an Er-doped laser.

The third option is to use wavelengths generated by non-linear effects. Frequency comb generation in a high-Q mode-locked cavity can generate a wide range of wavelengths from near-IR to mid-IR, and has the potential to cover the entire region of interest for obtaining a "gas fingerprint spectrum". By analyzing one pulse, we can obtain information about the full spectrum. Current work focus on high-efficiency comb generation, which requires thick stoichiometric silicon nitride film growth. **Chapter 4** shows the design and the successful fabrication of the material suitable for a comb device.

1.4. Integrated MIR Waveguide Sensor

Waveguide design and fabrication is the foundation of building the integrated sensing system. Chalcogenide glass is chosen due to its wide transparency window (from near-infrared up to 20 μm). How does it perform in a real gas sensing experiment? What limits the performances? All these questions are investigated in **Chapter 5** based on GeSbS material system.

Besides, to analyze the spectrum without changing the emission of the wavelength during the scan, one needs to guide the light into different wavelength-specific detectors. Optical switches which control the light path are one of the most important components of this optical router system, and one can make use of chalcogenide glasses which demonstrate an appropriate phase-change property for this application. Under certain drive currents or light exposures, the phase of a chalcogenide glass material can be switched between crystalline and amorphous. **Chapter 6** introduces an optical on/off switch design combining GeSbTe (GST) with plasma technology. The switch has nanometer-scale footprint and consumes low energy.

1.5. Integrated MIR detector

Chapter 7 discusses PbTe based detectors, which is proposed as a photoconductive detector for a monolithic integrated optical chip. The material property and fabrication techniques have previously been well examined by our group. In this work we use that know-how to successfully design, fabricate and test a waveguide-integrated on-chip MIR PbTe detector, the first of its kind..

At the end, a vision for the future of integrated MIR sensing is presented based on the innovations from this work. Also, specific future directions for the different components of the integrated sensing platform are analyzed.

Chapter 2. Germanium Light Source

2.1. Introduction

Bulk Ge has an indirect bandgap structure and a direct bandgap at the Γ valley (0.8 eV) is slightly larger than the indirect bandgap at the L valley (0.66 eV), as shown in Figure 2-1. To make it more "direct" to improve optical performance, we will engineer the material and change its band structure. Our target is to make more electrons stay in the direct Γ valley and emit photons. Shrinking the energy difference between the L valley and the Γ valley will help. Increasing the total electron number or energy of electrons are also possible approaches.

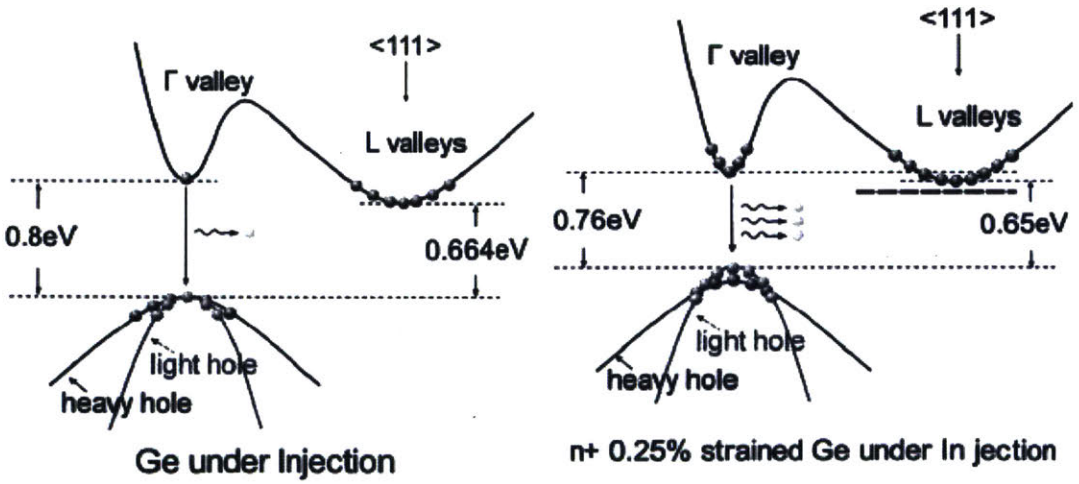

Figure 2-1 Ge band structure without strain (LHS) and with 0.25% tensile strain (RHS)

As mentioned before, there are several mechanisms to change the band structure of Ge. By adjusting these factors in Ge, we can get the desired target material which has a

small threshold current at a specific emission wavelength (for example, 1550 nm or even longer).

In this chapter, we will consider the following mechanisms: 1) Strain effect, which will change the energy of each valley. 2) Doping and injection effect, which can raise the quasi-Fermi level and, more importantly, cause band gap narrowing (BGN) and band gap renormalization (BGR) effects. Besides, the doped or injected free carriers will cause absorption. 3) Quantum confinement, which can change the total band structure and decrease the density of states (DOS) of the confined gamma valley. Lower gamma DOS means higher the differential gain and thus lower threshold current. The work in this chapter is based on 0.25% tensile strain Ge-on-Si platform and focuses on studying how these factors affect laser performance.

2.2. Strain Effect

When a crystal is under uniform deformation, it may preserve the periodic structure such that the Bloch theorem will still be applicable. But the new band structure will be slightly different from the original one due to new shape of elementary cell [14]. By applying $\boldsymbol{k} \cdot \boldsymbol{p}$ method, the variation energy at the band edge can be calculated. Due to different symmetry in reciprocal space and different wave function, the energy shifts of different valleys vary from each other.

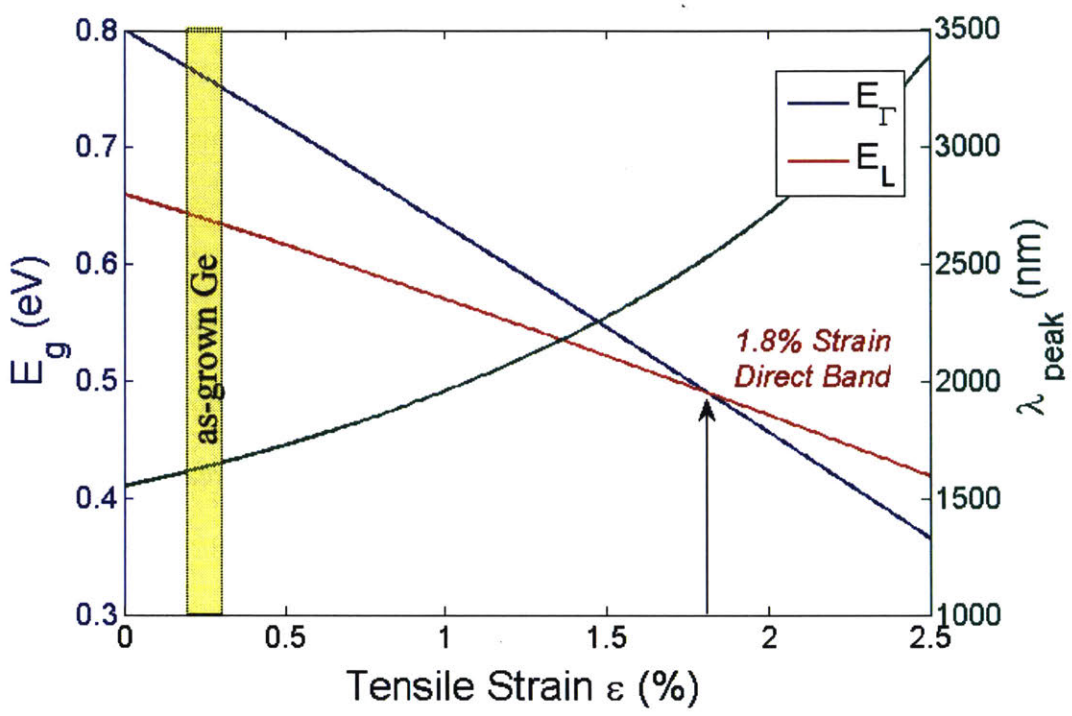

Figure 2-2 Germanium band structure change under biaxial tensile strain[15]

Under uniform tensile strain, conduction band energy will drop according to equation (2-1):

$$\Delta E_{\Gamma,L} = a_{c\Gamma,\mathrm{L}}(\varepsilon_{xx} + \varepsilon_{yy} + \varepsilon_{zz}) \tag{2-1}$$

ΔE_Γ and ΔE_L are energy shifts of Γ and L valley, respectively. And the negative constants $a_{c\Gamma}$ and $a_{c\mathrm{L}}$ are there deformation potential factors. ε_{xx}, ε_{yy} and ε_{zz} are strain. From both experiment and theoretical calculation, the decrease of the Γ valley is faster than that of the L valley[16]. 1.8% tensile strain can make Ge a "direct bandgap material" and shrink the bandgap to 0.53 eV, which is far from the communication wavelength (1550 nm, or 0.8 eV). For MIR applications like ours, higher strain is beneficial because

it makes the emission wavelength longer. However, strong strain will introduce dislocations and defects, thus new membrane technology is needed. Silicon nitride layer grown over the Ge structure can apply a high strain to the Ge layer[17,18].

2.3. Doping and Injection

With strain lower than 1.8%, Ge is not "direct". Most of the electrons will still stay in L valley. To get material gain for lasing, we have to create population inversion, that is, to raise the quasi-Fermi level in the conduction band and decrease the quasi-Fermi level of the valence band until their difference is larger than the direct bandgap. Thus both doping and injection are needed to change the relative quasi-Fermi level. N-type doping is preferable compared to hole injection because injected holes can generate huge free hole absorption, while the free electron absorption is almost negligible[13]. Thus to introduce the same quasi-Fermi level split, heavier doped samples will experience lower free carrier absorption, which is good for lasing condition. Due to the *in situ* doping solubility limit, current doping concentrations are insufficient for population inversion, thus high hole injection levels are still necessary.

However, the extra electrons in the conduction band will strongly interact with each other and with doped impurity ions. Such many-body effects can decrease the energy of conduction band and increase the energy of the valence band, thus shrinking the bandgap, which is undesirable for telecommunication applications. The wavelength of the emitted photon will be longer than the classical prediction. These effects are named band gap narrowing (BGN) or band gap renormalization (BGR) effects, depends on the source of the extra electrons.

BGN effect is caused by heavy doping[19]. As evidence, a shift in absorbed or emitted wavelength due to doping has been observed in many semiconductor materials, including unstrained Ge[20-23]. Berggren explained the mechanism of BGN under low temperature by combining the Hartree-Fock potential with correlated homogeneous electron gas screening and considered impurity scattering[24]. Jain improved the theory by introducing a much simpler equation and compared the simulation with data from absorption experiments[25]:

$$\Delta E_g = \Delta E_x + \Delta E_{cor(mino)} + (\Delta E_{i(maj)} + \Delta E_{i(mino)}) \quad (2\text{-}2)$$

In n-type semiconductors, exchange interaction ΔE_x is defined by the electron interactions in the different sub-bands, which is described by the Hartree-Fock potential. The electron-hole correlation energy $\Delta E_{cor(mino)}$ will result in shift of the holes; and the shift of electrons (majority carriers, maj) and holes (minority carriers, mino) due to carrier impurity interactions is represented by $\Delta E_{i(maj)}$ and $\Delta E_{i(mino)}$ respectively. Jain's theory shows good agreement with experiment data at low temperature for indirect bandgap of Ge from Haas [26]. However it cannot be applied to direct bandgap at high temperature [27].

BGR effect is caused by carrier injection. In fact, it also results from carrier exchange and correlation, which is similar as BGN[28]. The main difference is BGR has no impurity center scattering. Usually for Ge under heavy doping, the injected carrier density is small. Only BGN effect is considered. But for Ge lasing which requires both high doping and high injection, a combination of both effects is needed. It remains unknown how injected carriers and holes will be affected by impurity ions.

To study the doping effects on BGN effects for heavily doped Ge, Ge thin film is doped and measured by photoluminescence (PL). Germanium films were grown epitaxially on bulk silicon substrates with (100) orientation by ultra-high vacuum chemical vapor deposition (UHVCVD). Ge films were deposited in a two-step process, beginning with a low-temperature deposition of a thin but highly defective Ge buffer epitaxial layer. This buffer layer relaxes the strain induced by lattice mismatch of 4.2% between Si and Ge at the substrate interface and serves as a sink for dislocations. On top of the buffer layer, a high-temperature co-deposition of Ge and P creates a thick layer of high quality crystalline n^+ Ge with a carrier concentration of 1×10^{19} cm^{-3}. Then, delta doped Ge layers are deposited. They consist of monolayers of P encapsulated by intrinsic Ge. The upper cladding of the material is provided by a PECVD SiO_2 layer. P is diffused into the n^+ Ge film by rapid thermal anneal (RTA). The oxide layer acts as a diffusion barrier. The Ge threading dislocation density is $\sim 3 \times 10^8$ cm^{-2} in the delta doped region and $\sim 10^7$ cm^{-2} in the intrinsic doped Ge from TEM measurements. The point defect density is assumed to be $\sim 10^7$ cm^{-3} from the law of mass action.

Blanket films and waveguides were fabricated and then measured using x-ray diffraction (XRD) and PL. The different dopant concentrations were analyzed using SIMS, Hall Effect, and PL measurements. A Horiba MicroPL system utilizing a 1064nm laser with a maximum power density of ~0.05 $mW/\mu m^2$, and an EOS InGaAs IGA1.9 photodetector were used at room temperature (RT) to measure the photoluminescence spectra of the Ge samples. The detector cutoff is at ~2100 nm at RT. The samples were measured with a temperature control stage to eliminate extraneous effects such as lattice temperature increase.

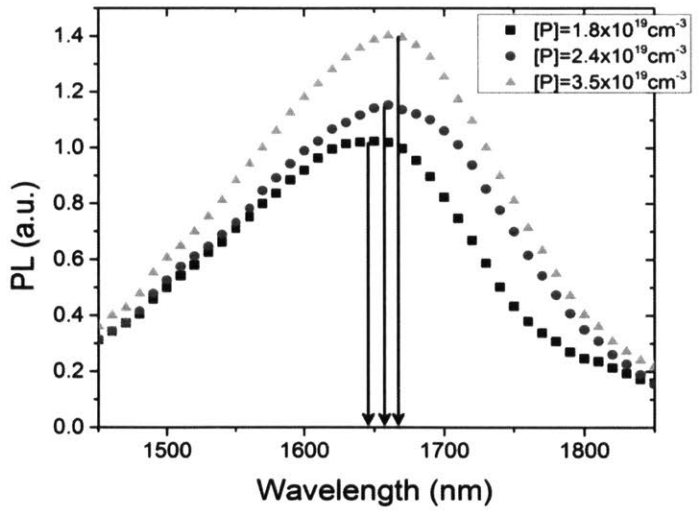

Figure 2-3 PL intensity for heavily n-type doped Ge. BGN shift in emission compared to doping concentration of samples analyzed. Arrows show peak shift from the different doping concentrations, red shifting with increasing active dopant[27].

Samples with P concentrations ranging from $5x10^{18}$ to $4.5x10^{19}$ cm^{-3} were studied. XRD measurements showed that both blanket films and waveguides have similar tensile strain of ~0.25%.

It has been shown, that an increase in PL intensity in Ge is equivalent to higher active carrier concentrations in Ge when retaining low defect concentration. SIMS and Hall effect measurements confirm that the dopants in Ge are fully activated, hence, they can be treated as free carriers capable of contributing to the direct band-gap emission. As expected, the total integrated PL emission also increases, indicating insignificant defect related traps, and confirming that active dopants are contributing to emission. In addition to such increase of PL intensity, we also observe a redshift of the peak wavelength for the direct band gap emission with higher doping concentration, as seen in Figure 2-3. The

PL emission originates from the band-edge of the direct Γ valley. Hence, the PL peak emission is equivalent to the energy gap, E_Γ, in agreement with previous calculations and experiments. The wavelength shift indicates BGN of the Ge Γ valley transition. Although change of strain may also result in a shift of the bandgap, cross-analysis with XRD shows that even at these high doping levels, dopant concentration used in these experiments are not sufficient to relax the lattice strain. We therefore consider a model only based on carrier interactions to explain such BGN effects. BGN also provides a simple, non-destructive measurement technique to determine doping concentrations of samples smaller than permitted for standard methods. Since the Fermi level is still below the Γ valley, Boltzmann distribution is used to interpret the emission spectrum. The energy of the peak emission is kT/2 higher than the direct bandgap. k is the Boltzmann factor and T the temperature. The band gap without BGN is calculated by adding kT/2 to the energy difference between valence band maximum and Γ-valley minimum. The difference between the PL peak emission for doped and undoped Ge provides the BGN in the Γ valley.

Haas presented his observation of direct BGN of Ge by analyzing the absorption spectrum[29]. This method takes into account recombination of carriers from valence band to L valley band edge. Both absorption and emission mechanisms show equivalent results for Γ valley at 300K, as shown in Figure 2-4. Our data fit Hass's 300K data and suggests a lower limit for BGN, as will be discussed. The extensive experiments in this work show a linear dependence of Γ-point band gap shrinkage with heavy n-doping.

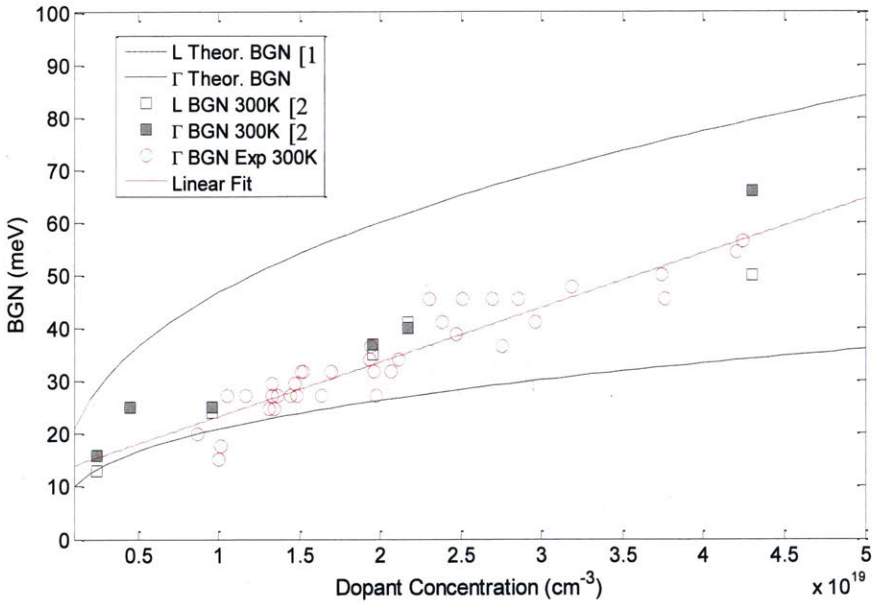

Figure 2-4 Experimental observations of BGN as a function of n-type doping concentrations at 300K. A linear relationship is observed. The data falls between Jain's theory (L band) and equation 4 of this work for the minimum change (Γ band).The inserted table shows parameters used in equation 2-5 and 2-6.

From first principles, theoretical treatment of the experiments in this work may need to consider two distinguishing features: i) the experiments were performed at 300K, and ii) Ge is tensile strained moving L- and Γ- band minima closer together. This approach might be generalized for Ge according to Equation 2-3,

$$E_g(N_D = 0) - E_g = E_{BGN} + \Delta_{BGN} N_D(cm^{-3}) \tag{2-3}$$

where N_D is the dopant concentration, E_{BGN} is Δ_{BGN} turn-on offset energy reduction (intercept of the linear relationship at ND=0); and Δ_{BGN} is the BGN coupling parameter

(slope of the linear dependence of E_g reduction with N_D). The data of this work yield the following parameters: E_{BGN}=0.013 eV and $\Delta_{BGN}=10^{-21}$ eV/cm^{-3}.

We propose that the linear dependence can be regarded as the dominant first order term of a BGN phenomenological model. The linear fit, therefore, can be used to predict with reasonable accuracy the spontaneous emission wavelength of doped Ge and to measure through such emission the doping level of the Ge.

This functional dependence contrasts with predictions of the Jain model for the L-valleys and of the simplified lower-limit model further discussed in this work. However, the experimental values of all observations fall between the predictions of the two models.

Jain's model for BGN assumes a static lattice model for temperatures <77K. It has four components [25]:

$$\Delta E_g = \Delta E_x + \Delta E_{cor(min)} + (\Delta E_{i(maj)} + \Delta E_{i(min)}) \tag{2-4}$$

In n-type semiconductors, the exchange interaction, ΔE_x, is defined by the electron interactions in the different sub-bands, which is described by Hartree-Fock potentials 14. The shift of the holes is considered in the electron-hole correlation energy, $\Delta E_{cor(min)}$; and the shift of electrons(maj) and holes (min) due to carrier impurity interactions is represented by $\Delta E_{imp}=\Delta E_{i(maj)} + \Delta E_{i(min)}$. If the shift of the L valley is considered, the equation has the following form [25],

$$\frac{\Delta E_g}{R} = 1.83\frac{\Lambda}{N_b^{1/3}}\frac{\delta}{r_s} + \frac{0.95}{r_s^{3/4}} + \left[\delta + \frac{R_{(min)}}{R}\right]\frac{1.57}{N_b r_s^{3/2}} \tag{2-5}$$

where N_b is the number of interacting sub-bands, Λ is the correction factor due to anisotropy in the conduction band; R is the effective Rydberg energy for both majority (R) and minority carriers (R_{min}); and r_s is an dimensionless unit from the half average distance between impurities, r_a, under the effective Bohr radius, a.

In the classic low-temperature model, inter-valley interaction is limited and electrons can only have exchange and scattering effects within their own sub-valley. Such effect in the L valleys is much larger than that for the Γ valley, reducing ΔE_x and $\Delta E_{i(maj)}$ for the Γ valley. Thus for the Γ valley only the correlation energy $\Delta E_{cor(min)}$ and the impurities interaction of valence band $\Delta E_{i(min)}$ are left in the equation. Since $\Delta E_{cor(min)}$ and $\Delta E_{i(min)}$ reflect only changes on the energy of states in the valence band, the same values can be used for L and Γ valleys. The equation becomes,

$$\Delta E_{\Gamma} = 8.15\left(\frac{N}{10^{18}}\right)^{\frac{1}{4}} + 2.03\left(\frac{N}{10^{18}}\right)^{\frac{1}{2}} \quad (2\text{-}6)$$

This equation expresses the unique contribution of carrier concentration to the shrinkage of the band gap at the Γ point in Ge. This expression should be regarded as the minimum band gap shrinkage because carrier redistribution due to higher temperatures will further reduced the band gap. As seen in Figure 2-4, the ΔE_{Γ} prediction is undervalued at 300K.

At 300K an increase of doping concentration clearly narrows the band gap, and the energy reduction follows a linear relationship with doping. It is significant to observe that Hass's data for both L and Γ BGN, and our data follow the same linear relationship at 300K, as seen from Figure 1.3. In this context, the similar BGN effects observed by Hass for the Γ-point and L-points conflicts with Pankove[30] have modified k-space theory. One

possible reason is that more electrons will go into the Γ valley at high doping and that temperature may generate a larger exchange interaction, ΔE_x. Another possible reason is the effect of impurity band formation at high doping. An impurity band would enhance the interaction between electrons in L and Γ valleys, weaken momentum conservation, and may average the energy shift in different valleys. Thermal energy can also increase interaction between Γ and L valleys by providing energy for intervalley scattering transitions.

From our PL results, the peak emission shift reflects the free carrier concentration and, since all dopants are activated, the dopants concentration. By using Equation 1, we can determine the active dopant concentration by analysis of the PL spectrum, and vice versa. Within the tensile strain values studied in our Ge films of 0-0.3%, we find no evidence that doping induced BGN is modified by strain.

Our work shows that BGN measured from a PL spectrum can be used as a nondestructive technique to determine active carrier concentrations in heavily doped Ge. This technique could be extended to other semiconductors with similar behavior.

In summary, we measure significant red-shifts in the photoluminescence spectra of degenerately n-doped, tensile strained Ge. The red-shift exhibits a linear dependence on doping level that we have interpreted as band gap narrowing, BGN. We propose a first order phenomenological model for BGN based two parameters whose values for Ge are E_{BGN} = 0.013 eV and $\Delta_{BGN} = 10^{-21}$ eV/cm^{-3}. BGN can be a powerful non-destructive method for determining the total active dopant concentration in Ge-on-Si devices, as well changing the emission wavelength to push the Ge light source into the MIR range.

2.4. Quantum Confinement

While III-V quantum well structures have achieved great success in high performance lasers, Ge nanostructures typically have a type-II band alignment with the Si barrier layer, which prevents effective quantum confinement of carriers in Ge. As a result, most of the luminescence from Ge-on-Si nanostructures actually originates from the indirect recombination of electrons in the Δ valleys of Si with the holes in Ge, which is much less efficient than type I quantum confined structures[31]. Even though type I alignment can be achieved using $Si_{0.15}Ge_{0.85}$ barrier layers[11], as shown in Figure 2-5, the quantum confinement raises the energy of the Γ valley much more than the L valleys since the Γ valley has a much smaller effective mass (0.038 vs. 0.2 m_0) and the band-offset of the Γ valley is much larger than that of the L-valleys (0.53 eV vs. 0.18 eV). These two factors lead to a larger energy difference between Γ and L valleys and adversely affect the direct gap emission. Assuming that the BGN effect in QWs is similar to the bulk material, Figure 2-6 reveals that, with the decrease of QW width, more electrons are needed to raise the quasi-Fermi level to the lowest energy level of the Γ valley.

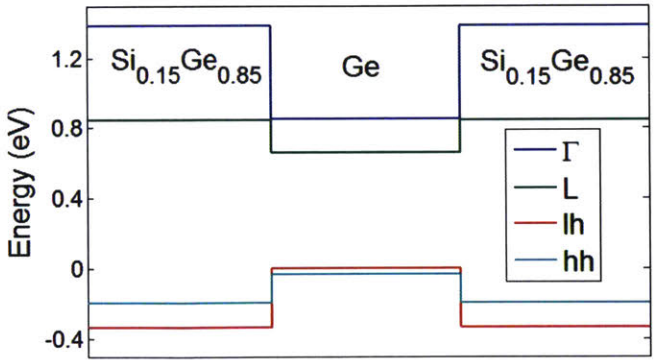

Figure 2-5 Current $Ge_{0.85}Si_{0.15}$/Ge/$Ge_{0.85}Si_{0.15}$ MQW band structure assuming 0.25% tensile strain in Ge QW[32].

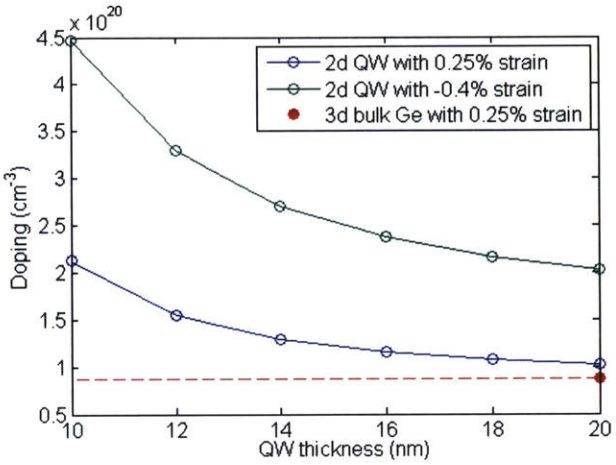

Figure 2-6 Density of electrons needed to raise the Fermi level to the lowest energy state in Γ valley. Strain effect is included. The -0.4% strain represents strain condition of Ge in $Ge_{0.85}Si_{0.15}$/Ge/$Ge_{0.85}Si_{0.15}$ QWs shown in Figure 2-5.

Simulation results in Figure 2-7 further show that in Ge/SiGe QWs there is hardly any decrease in injected carrier density needed to make Ge transparent. It is because of the competition between two mechanisms: decreasing DOS in the Γ valley due to

quantum confinement makes population inversion easier, yet more electrons are needed to raise the Fermi level as mentioned before. These two mechanisms largely cancel each other resulting in only a slight decrease of n_0. Although we cannot currently create SiGe/Ge QWs with tensile strain, if we assume it is possible to use 11.8 nm MQW with 0.25% tensile strain as active material and use the same laser structure as for bulk Ge, we can calculate threshold current with varying numbers of QW layers, as shown in Figure 2-8. The thickness of the QW is chosen for lowest transparency n_0 at 1550 nm. Increasing the number of QW layers will increase the optical confinement factor but also increases the thickness of active material and change the absorption. This tradeoff results in the lowest threshold current for a 4-layer QW structure.

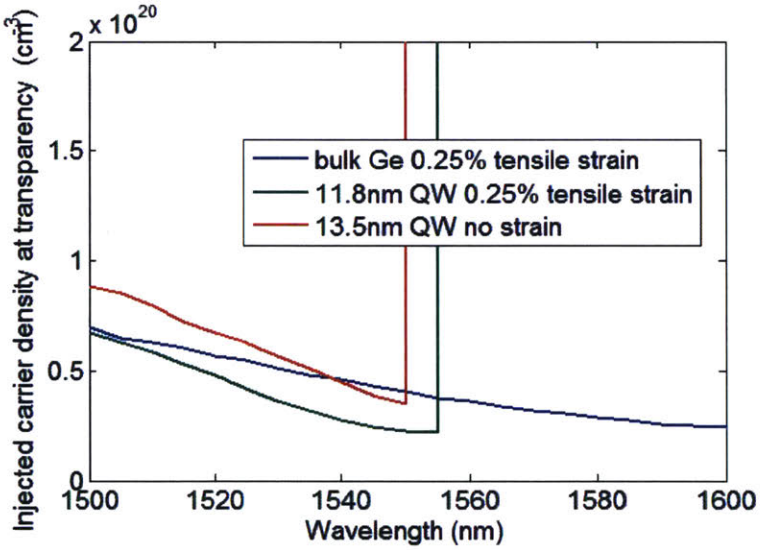

Figure 2-7 Injected carrier density at transparency n_0 vs. wavelength of both bulk Ge and Ge QWs. Effects of BGN and strain are included. The thickness of the QW is chosen for lowest n_0 at 1550 nm. Tensile strain and QW can decrease n0, thus decrease threshold current. Note that this is an optimistic estimate for QWs since in reality they

are compressively strained. N-type doping concentration is 4.5×10^{19} cm^{-3}. No data here for 0.4% compressive strain QWs because transparency cannot be reached under any injection at such doping concentration.

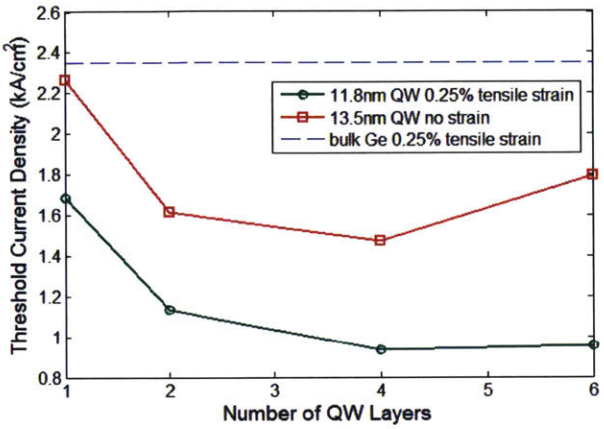

Figure 2-8 Calculated threshold current density at 1550 nm of QWs with and without tensile strain for different number of QW layers. The result is compared with threshold current of bulk Ge.

However, in reality epitaxial Ge nanostructures on Si or Si_xGe_{1-x} are usually compressively strained due to the lattice mismatch. Contrary to tensile strain, compressive strain adversely affects the light emission efficiency of Ge by further increasing the difference between the direct and indirect gaps of Ge [12]. As shown in Figure 2-7 and Figure 2-8, considering the compressive strain in realistic $Ge/Si_{0.15}Ge_{0.85}$ QW structures the n-type doping level and injected carrier density at transparency are even higher than bulk Ge materials. Even for MQW laser without strain at 1550 nm, the best threshold current is around 1.5 kA/cm^2, which is higher than that with tensile strain. Therefore, engineering tensile strain into Ge QWs by other stressor layers is critical for

the lasing performance. Considering the defects and doping difficulties while growing QWs, it is also important to resolve the fabrication issues to fully exploit the potential benefits of Ge QW lasers.

A possible alternative structure to QWs is quantum dots (QDs). Unlike III-V QDs, it has been shown both theoretically [33] and experimentally [34] that Si and Ge intermix extensively upon 3D QD formation, which further increases the difference between the direct and indirect gaps. Although some theoretical simulations predict certain direct gap Ge or SiGe nanostructures at very small dimension (<2 nm) [35] and some experimental studies reported direct gap Ge nanostructures by analyzing the absorption spectrum [36], so far no convincing evidence on direct gap light emission from Ge-on-Si nanostructures has been demonstrated. Most PL measurements on Ge-on-Si nanodots were performed at low temperatures and they still show indirect gap emission features that involve no-phonon (NP) and transverse optical (TO) phonon transitions. Although the oscillation strength of NP transition and the overlap of electron and hole wave functions are enhanced in Ge/Si nanostructures, they are still orders of magnitude less efficient than real direct gap transitions [37,38].

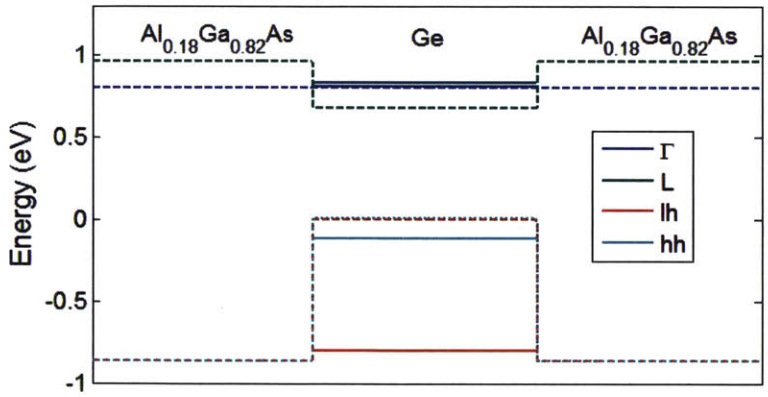

Figure 2-9 Band structures of possible AlGaAs/Ge/AlGaAs QWs. The thickness of Ge is 3.3nm. For different valleys, dashed lines show the band edges and solid lines show the 1st energy level in the wells. Barrier material is chosen so that there is no quantum confinement in Γ valley. Assume no strain and BGN effects.

Although there are obstacles in traditional Ge quantum device on Si or Si_xGe_{1-x}, there are other possibilities to improve quantum enhancement of light emission in Ge device. Previous theoretical [39] and experimental results have shown that when the size of Ge nanocrystals embedded in SiO_2 is decreased below 3 nm, significant Γ-L mixing takes place due to the strong localization, leading to a dramatic decrease in the radiative recombination lifetime. Takeoka et al. [40] reported a fast PL decay component ($<<1\mu s$) for Ge dots ranging from 1.2-3.2 nm in diameter superimposed on a slow component lasting microseconds. The contribution of the slow component decreases with the dot size, and at the same time the PL intensity increased, indicating an indirect-to-direct transition. Saito et al. also observed similar emission from ultrathin Ge or Si on SiO_2 as well as ultrathin fin structures [41]. A significant challenge though, is electrical injection into these

structures. Ge nanocrystals in SiO_2 suffer from an insulating matrix, while lateral injection into ultrathin Ge layers or fins tends to have a high series resistance. To overcome these issues and further improve the performance of Ge lasers, here we propose a "separate electron barrier" approach, where the barrier material provides strong confinement in L valley, but weak confinement in Γ valley. This idea can be implemented by carefully choosing the barrier material that provides a large band-offset in L valleys while small off-set in Γ valley with Ge. Such band alignment can make Germanium "direct bandgap material" by raising L valley's lowest excited state in Ge closer to or above the Γ valley due to quantum confinement of electrons in L valley. In this case direct bandgap material is needed as barrier layer, such as AlGaAs. As an example, the band diagram of a AlGaAs/Ge/AlGaAs QW structure is shown in Figure 2-9 where the Ge QW is converted into a direct gap material. One could also tweak the design to engineer the L valley slightly below Γ valley for high lasing performance at elevated temperatures. There are several advantages to do this approach: (1) The AlGaAs barrier layer is not an active material but just a barrier layer electrode, so it can be deposited at low temperature to avoid diffusion of III and V elements and achieve CMOS compatibility. (2) Off-cut wafers are not needed either since antiphase boundaries will not affect performance in this case. (3) Pseudo-direct gap Ge lasers offer much better thermal stability, and in this case one can engineer the relative positions of L and Γ valleys by QW design for optimal performance. In III-V lasers QD lasers can also show such good thermal stability, but the wavelength of these QDs is far from 1550 nm and they have not been integrated on Si so far. Therefore, this new Ge QW design could offer a simple solution to high-performance monolithic lasers on Si at 1500-1700 nm.

In summary, quantum well structure will limit the performance of Ge laser. It makes the material more "indirect" as well as increases the bandgap, which is a disadvantage for MIR sensing applications.

Chapter 3. Rare-earth Doped Chalcogenide Light Source

3.1. Introduction

Obtaining lasing in the mid-IR regime has been a challenging task, and the invention of quantum cascaded lasers (QCLs) [42] represents a revolutionary development in this area. However, near the short-wavelength end of the mid-IR range, around 2~4 μm, the availability of QCLs is quite limited. Another technical approach to lasing at the mid-IR, which has also experienced great advances recently, is rare-earth-doped fiber lasers. Silica fiber becomes a mature host for rare-earth dopants around 2 μm, while chalcogenide glasses are chosen for a wavelength beyond 3 μm in many cases[43] due to their low phonon energies for a wide infrared transparency window and low non-radiative decay rates for high quantum efficiency in lasing. A 3.5 μm fiber laser has been demonstrated in Er^{3+}-doped ZBLAN glass [44]. However, the refractive index of ZBLAN glass is relatively small, which limits the choices of substrates for an integrated on-chip laser[45]. A good host material for an Er-doped planar laser is gallium lanthanum sulphide (GLS), since it exhibits high refractive index, no toxicity, no hygroscopicity, low phonon energy and low non-radiative decay rate [43].

Transferring the mid-IR solid-state fiber laser technology to an integrated device configuration would be a critical step to build an on-chip mid-IR laser. The first proposal was published in 2011 [46], in which a microdisk resonator is simulated for building an Er-doped mid-IR laser at 4.5 μm, with an optical pump at 0.8 μm. However, in that early work, cavity design was simplified. For example, it was assumed that coupling between

the disk and waveguides can be perfect to achieve a high-Q cavity.

Several specific design issues need to be considered in the case of an integrated Er-doped mid-IR laser cavity. First, the device has to support guided modes at both pump and signal wavelengths, which are separated by a spectral spacing of more than two octaves (e.g., the pump is near the edge of the visible range, and the signal is in the mid-IR, 3~5 μm). This means that the device has a large number of higher-order modes at the pump wavelength, and input pump can be coupled to many of these modes simultaneously. Therefore, special attention is required in the cavity design. Second, the pump must be efficiently injected into the cavity, and thus a certain coupling strength is required, made possible by placing an input waveguide close to the cavity. However, the signal wave will have much stronger coupling due to its increased evanescent field and easily escape from the cavity, which may cause a cavity loss greater than the round-trip gain and prevent the device from lasing. Third, a large resonance-enabled power enhancement is highly desired at the pump wavelength, making it possible to greatly reduce the input pump power so that widely available visible optical sources can be used as a pump. This requires the cavity to be operated near critical coupling with a high cavity Q-factor at the pump. On the other hand, the Q-factor at the signal wavelength needs to be tailored such that cavity coupling to a waveguide can control lasing threshold and differential gain. To the best of our knowledge, these challenging issues in designing an integrated rare-earth-doped mid-IR laser have not yet been addressed.

In next section, we numerically demonstrate the feasibility of building a planar room-temperature low-pump-power integrated mid-IR laser, enabled by a high-Q

microresonator. Essentially, the cavity acts as a microring resonator at the signal wavelength in the mid-IR range and is similar to a whispering gallery microdisk resonator at the pump wavelength. With a clever design of the cavity, we significantly reduce excitation and mixing of higher-order modes at pump wavelength, while simultaneously reducing the external coupling of the cavity at signal wavelength by using a single coupler for both pump injection and signal output. In this way, the resonator exhibits a high cavity Q-factor greater than 10^5 at both pump and signal wavelengths. The pump threshold can be reduced to remain below 10 μW.

3.2. Er-doped Chalcogenide Glass Laser Design

In addition to material property advantages of Er^{3+}-doped GLS glass as stated above, this material system has been well studied and we have sufficient data including transition rates[19]. So in our work here, we utilize Er^{3+}-doped GLS glass [43]to test our structure. Bulk Er^{3+}-doped GLS shows mid-IR photoluminescence emission at 3.6 μm through the transition between $^4F_{9/2}$ and $^4I_{9/2}$ energy levels, as shown in Figure 3-1 (a). The correlated pumping wavelength is 0.66 μm, and the signal wavelength is 3.6 μm. The 0.66 μm pump can be realized by a semiconductor laser. One may argue that the lifetime of the $^4F_{9/2}$ level (0.11 ms) is smaller than that of the $^4I_{9/2}$ level (0.59 ms), thus preventing lasing. However, detailed analysis based on transition rates [19] shows that lasing can occur, and will be proved at the end of this section. Er^{3+}-doped ZBLAN has advantages in lifetime and quantum efficiency, and will be a promising candidate in the future if an appropriate low-index substrate (n ~ 1.5 for both pump and signal wavelength) can be identified.

GLS is capable of hosting relatively high erbium concentrations (2.8×10^{20} ions/cm^3) without luminescence quenching. However, the maximum gain is still limited by the emission cross-section to about 4 dB/cm [43]. Therefore, for lasing under this constraint, a high cavity Q-factor for signal wavelength is required. Moreover, to decrease the threshold and increase quantum efficiency, a high power enhancement factor of pumping light is also necessary, which is defined by the equation:

$$\eta = P_{ring}/P_{bus}$$

where P_{ring} is the optical power inside the resonator, and P_{bus} is that in the bus waveguide.

To address the design issues mentioned above and enhance the cavity Q-factor at these widely separated wavelengths, it is important to manage wavelength-dependent coupling. We bend the bus waveguide along the laser cavity so that we have more control knobs to use, as shown in Figure 3-1(b). Some general ideas and considerations have been incorporated into the cavity design.

First, the cavity has to support the fundamental mode at 3.6 μm with a waveguide width comparable to the wavelength in the core material (i.e., wavelength divided by material index of refraction). In this way, the second-order mode at 3.6 μm is cut-off to increase the Q-factor of the fundamental mode. On the other hand, the input waveguide should be narrow enough that the incoming pump light as a fundamental mode at 0.66 μm has a relatively large evanescent field for efficiently coupling the pump power in. This means that the coupler between the cavity and the input waveguide is highly

asymmetric.

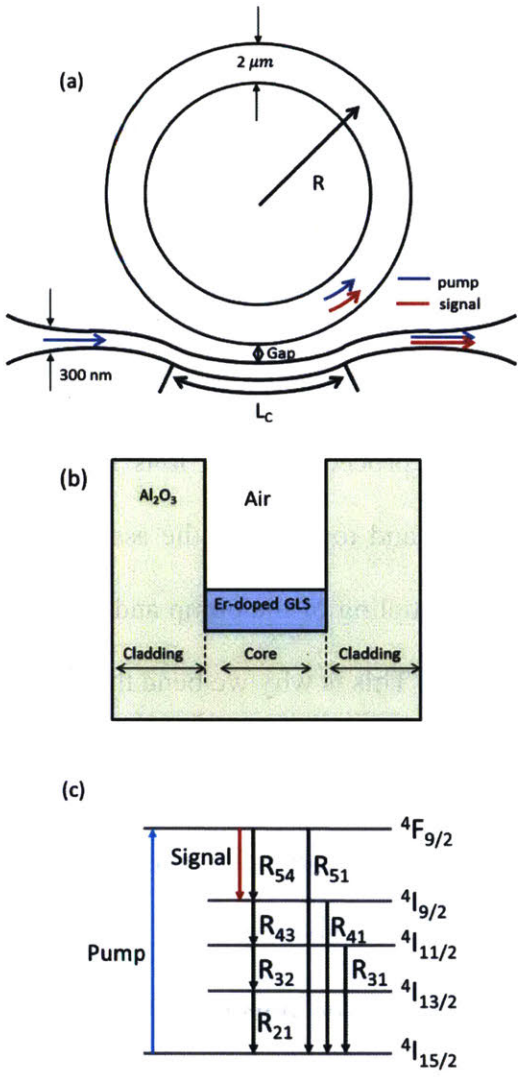

Figure 3-1 (a) Device configuration of a high-Q microresonator-based mid-IR laser, which consists of a multi-mode ring resonator with a curved bus waveguide. (b) Cross section of a chalcogenide waveguide that is in an Al_2O_3 trench. (c) Er energy levels and inter-level transition parameters. From bottom to top is energy level No. 1 to 5.

Second, the waveguide that forms the cavity is highly multimoded at 0.66 μm. The incoming pump can excite many of the modes and transfer energy to them. However, these modes will not be in resonance simultaneously and will be mostly lost when traveling along the cavity. It would be better to excite as few modes as possible in the coupling area. In this sense, we avoid using a race-track ring structure, because otherwise near the junction between the curved and straight sections of the cavity, the structural perturbation (i.e., the junction) inevitably excites many undesired modes.

Third, one can add a waveguide for coupling the signal out, as in [46]. This may be convenient in terms of design procedures, but it is not favorable to reduce the total external coupling of the signal and to enhance the associated Q-factor. Thus, we use a single waveguide for both in-coupling of the pump and out-coupling of the signal, which requires greater design freedom. This is why we bend the waveguide.

Fourth, it is important to note that, since the waveguide is also used to couple the mid-IR signal out of the cavity, the waveguide needs to be widened adiabatically to have a signal mode better confined inside the waveguide. Therefore, before the coupling area, the waveguide should be designed for enhancing the light injection of the pump, but beyond the coupling area we should modify the waveguide to better deliver the signal by tapering its width.

In the simulation, the radius of the ring resonator, R, is set to 80 μm to produce a low bending loss. The thickness of the Er^{3+}-doped GLS layer is 0.5 μm and the width of the ring resonator is 2 μm to make it a single-mode waveguide for the mid-IR signal. The bus waveguide consists of three arc sections and two straight sections, with a width of 300

nm, as shown in Figure 3-1 (b). The gap width and coupling length L_C vary in our design to optimize the Q factor at the signal wavelength as well as power enhancement factor, η, at the pump wavelength.

To suppress sidewall scattering loss, lift-off is usually used for chalcogenide glass devices. Although it has been claimed that an Er^{3+}-doped GLS device can be made by lift-off technology, the photoresist is not removed after fabrication, which will strongly absorb mid-IR signal light. Lift-off technology for GLS is still under development. To avoid using lift-off, we propose trench-growth technology, which is similar to the lift-off scheme without needing to remove the patterning layer. A sapphire wafer can be used as a substrate, because it is transparent at both the pump and signal wavelengths. A 2-μm-deep trench is etched followed by the sputter deposition of a 500-nm-thick Er3+-doped GLS film, as shown in Figure 3-1 (c). With this fabrication process, the guided mode within the active material inside the trench is well-isolated from the outside.

To simulate the above device, we first use the effective-index method to convert this 3D structure to a 2D one. The key material parameters are listed in Table 3-1.

The 2D structure as shown in Figure 3-1 (b) is simulated using a finite-element software package (COMSOL Multiphysics) in its stationary mode. The S-parameters can be extracted from the simulations as a function of optical wavelength near the pump and the signal, which allows us to find the loaded cavity Q-factors. Moreover, the resonance-induced power enhancement factor can also be extracted versus wavelength. .

Table 3-1 Material refractive indices used in simulation[47]

Parameters	at 0.66 μm	at 3.6 μm
Al_2O_3 index	1.765	1.700
Er-doped GLS index	2.457	2.354
Cladding effective index	1.765	1.700
Core effective index	2.399	1.926

The intrinsic loss including GLS absorption and sidewall scattering loss are critical in the determination of cavity Q-factor and laser performance. In fact, the scattering loss currently remains unknown from literature. Here, we use loss measurement results from GLS optical fibers, given in [48], which are 0.15 dB/cm for 3.6 μm and 1.5 dB/cm for 0.66 μm. These loss numbers are translated as the imaginary part of the refractive index and plugged into the finite-element model. Other loss sources, e.g., bending loss and coupling loss, are inherently included in the 2D simulations and can be reduced by design improvement.

To examine the laser performance, we use a five-level model. The energy levels and transition parameters are shown in Figure 3-1 (a). The laser performance is calculated according to the following rate equations:

$$\frac{dN_1}{dt} = \sigma_p \Phi_p (N_5 - N_1) + R_{51}N_5 + R_{41}N_4 + R_{31}N_3 + R_{21}N_2$$

$$\frac{dN_2}{dt} = R_{32}N_3 - R_{21}N_2$$

$$\frac{dN_3}{dt} = R_{43}N_4 - R_{32}N_3 - R_{31}N_3$$

$$\frac{dN_4}{dt} = \sigma_s \Phi_s (N_5 - N_4) + R_{54}N_5 - R_{43}N_4 - R_{41}N_4$$

$$\frac{dN_5}{dt} = \sigma_p \Phi_p (N_1 - N_5) + \sigma_s \Phi_s (N_4 - N_5) - R_{54}N_5 - R_{51}N_5$$

$$\sum_{i=1}^{5} N_i = N_{Total}$$

where N_i is the ion concentration at energy level i, and $\Phi_{s/p}$ is the signal or pump beam flux density, $\sigma_{s/p}$ is the signal or pump beam emission/absorption cross section, R_{ij} is the spontaneous decay rate from energy level i to energy level j, and N_{Total} is the total erbium doping concentration. All the transition rates are given in [19]. Using this rate equation model, one can examine the lasing threshold and differential gain of the laser.

As we discussed before, the lifetime of $^4F_{9/2}$ is smaller than that of $^4I_{9/2}$. This is due to the fast transition rate R_{51}. But lifetime is not the determining factor for lasing. From the equations above, we can find that at equilibrium before lasing:

$$0 = \frac{dN_4}{dt} = N_5 \cdot R_{54} - N_4 \cdot R_{4,tot}$$

Where $R_{4,tot} = R_{41} + R_{42} + R_{43}$. To reach population inversion condition, we need $N_5 > N_4$. The system can lase as long as we have $R_{54} < R_{4,tot}$. For our case[19], R_{54} ($370\ s^{-1}$) is smaller than $R_{4,tot}$ ($1695\ s^{-1}$). Therefore lasing is possible.

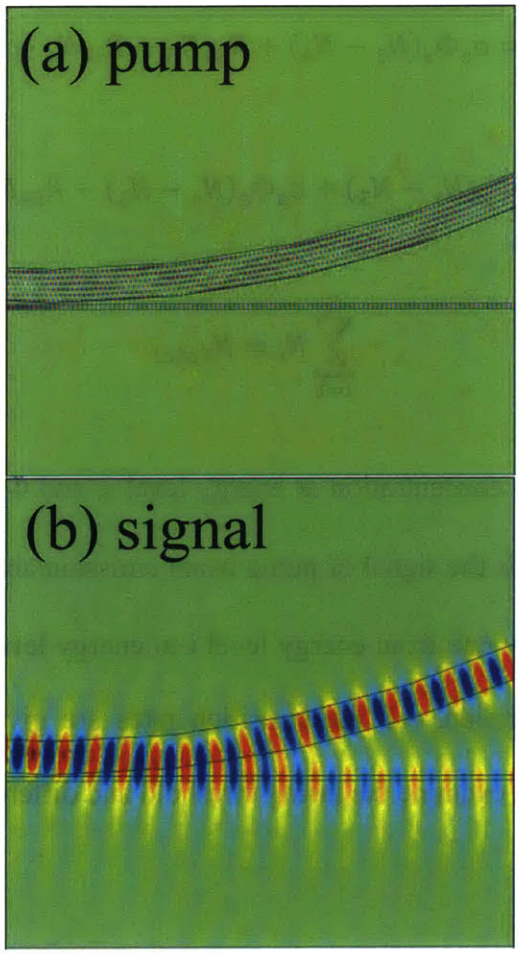

Figure 3-2 On-resonance mode field distributions: (a) at 0.66μm, the 6th-order mode is found, with quite uniform amplitude along the ring waveguide, due to a good isolation from other resonant modes. (b) at 3.6μm, we see single-mode light propagation, and

the bus waveguide at the right side needs to be widened after the ring and bus waveguides are spatially separated further.

In the cavity design based on the device configuration shown in Figure 3-1, we have in total five structural parameters to tailor. First, regarding the bending radius of the cavity, a large R helps reduce the bending loss but also reduces the free spectral range of resonant modes, which causes a larger number of mode crossings between different mode families. In other words, multiple modes will be excited and mixed, associated with a high cavity loss. A smaller radius will result in larger bending loss and increase the threshold power. If the radius goes down to 50 μm, the Q factor for signal wavelength drops to around 5000. We optimize R to be 80 μm in this work after considering the trade-off. The ring waveguide width is set to be 2 μm so that the second-order mode at 3.6 μm is cut off. Varying the bus waveguide width has an equivalent effect on coupling as does a change in coupling gap. Therefore, we mainly focus on the effects of changing the coupling length L_c and the gap.

We show the mode field distributions inside the cavity in Figure 3-2 for the TE modes at different wavelengths. At 0.66 μm, the 6th-order mode is chosen as shown in Figure 3-2 (a), which has a resonant peak well-isolated from other modes. The cavity is more like a disk resonator: higher-order modes are excited. From the analysis [46], we note that the higher-order modes are preferred for pumping light, because of a better overlap with the fundamental mode at the signal wavelength, which spreads more widely than the fundamental mode at the pump. The waveguide is more uniformly pumped by a higher-

order mode, which thus helps lasing. On the other hand, at 3.6 μm, the ring waveguide is single-moded, with the mode distribution shown in Figure 3-2 (b).

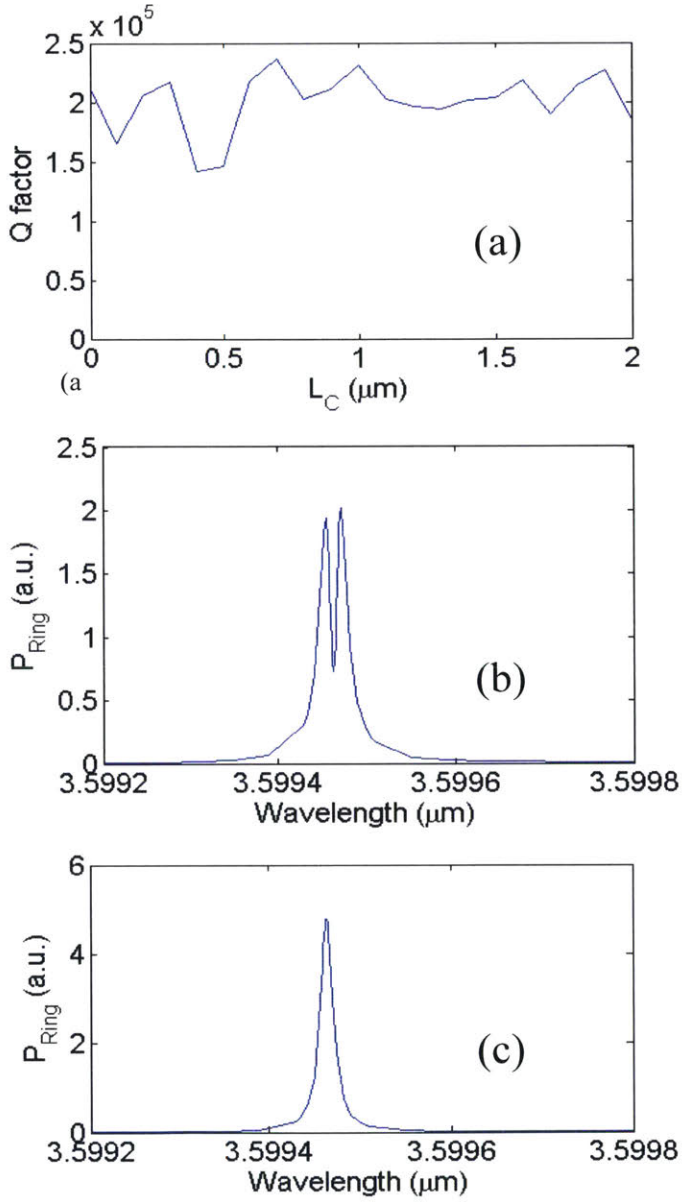

Figure 3-3 For a gap of 100 nm, (a) Q factor vs. L_C at the signal wavelength, i.e., 3.6 μm, Q-factor fluctuation is seen due to reflection-induced resonance mode splitting. We also show the intra-cavity power flow near the resonance as a function of

wavelength with (e.g., at L_C =0.4 μm shown in (b)) and without (e.g., at L_C =0.9 μm shown in (c)) the resonance mode splitting effect.

We vary the coupling length L_C and calculate the Q factor for a gap of 100 nm, as shown in Figure 3-3(a). The results show a Q-factor fluctuation around 2×10^5 at the signal wavelength, with several small Q-factor values caused by the mode splitting effect due to intra-cavity light reflection. When light travels inside the ring resonator, due to the strong perturbation in the asymmetric coupler, part of it reflects back. Although structurally this is a single resonator, physically there are two counter-propagating resonant modes that are coupled to each other due to the reflection, which causes two resonant peaks, i.e., so-called mode splitting. This effect broadens the composite resonant peak and decreases the Q factor. For example, at L_C=0.4 μm where Q factor drops to around 1.5×10^5. When we plot the power flow inside the resonator as a function of wavelength in Figure 3-3(b), we can see a sharp valley. This is because the counter-propagating optical waves have their power flow partially cancelled thus generating a standing wave. This phenomenon cannot be observed for some other coupling lengths, e.g., for L_C=0.9 μm, which is associated with standard Lorentzian-shaped resonance peaks in Figure 3-3(c).

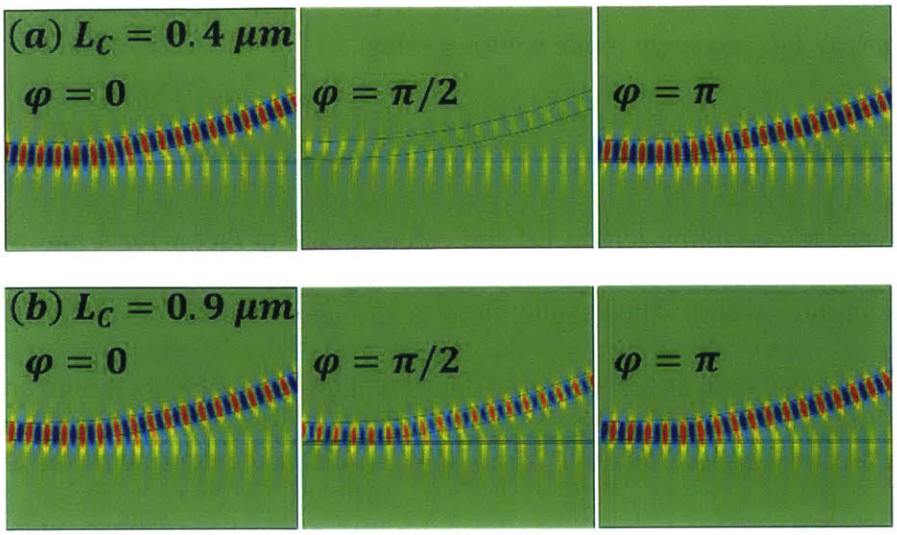

Figure 3-4 Mode field distributions show that standing-wave is formed at L_C =0.4 μm due to light reflection inside the cavity in (a), and the field distribution experiences zero with an optical phase φ=π/2. (b) At L_C =0.9 μm, the field distribution has a nearly constant amplitude as the optical phase changes with time.

To confirm the existence of the counter-propagating waves, Figure 3-4 illustrates the standing-wave nature of the mode field distribution at different times (i.e., optical phases). For L_C=0.4 μm, at the wavelength corresponding to the valley in Figure 3-3(b), the instantaneous amplitude of electromagnetic oscillations becomes almost zero for an optical phase φ=π/2, as shown in Figure 3-4(a). In contrast, for L_C=0.9 μm in Figure 3-4(b), at the resonant wavelength, the instantaneous amplitude remains almost constant for different optical phases, with little reflection.

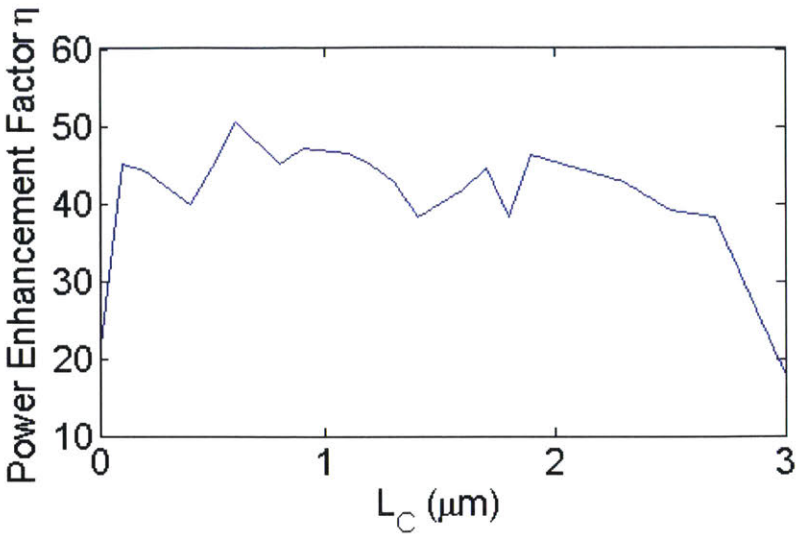

Figure 3-5 Power enhancement factor of the 6th-order mode at 0.66 μm changes with coupling length Lc for a gap of 100 nm.

At the pump wavelength (0.66 μm), our goal is to obtain a large power enhancement factor η instead of a high Q-factor. The simulation results are shown in Figure 3-5. The 6th-order mode is selected, because it is the highest-order mode that can be found without mixing with other resonant modes and it overlaps better with the signal mode. The power enhancement factor also slightly fluctuates due to the light reflection, as in Figure 3-3(a). As L_C increases, the 6th-order mode becomes very close to the critical coupling first, resulting in an increased η value. Then with a larger L_C, the resonator becomes over-coupled for the 6th-order mode, showing a drop of the power enhancement factor. The peak η value is 50.64 at L_C=0.6 μm.

From Figure 3-3 and Figure 3-5, one can see that, for a gap of 100 nm between the cavity and the bus waveguide, a high cavity Q-factor at the signal wavelength and strong

power enhancement at the pump wavelength are obtained, which do not sensitively depend on the coupling length L_C. Note that in this case the desired L_C can be as small as 0.6 μm, which means that the bus waveguide is essentially a straight waveguide.

The 100-nm gap can be realized by current 193 nm lithography. To exam the design tolerance and effects of gap width change, we also investigate the case with a gap of 200 nm. We see that the coupling, especially for the pump, becomes much weaker than that with a gap of 100 nm, and thus one has to increase L_C significantly. At the signal wavelength, the increased L_C causes the cavity Q-factor to decrease with L_C, peaking at 5 μm, which is comparable to those shown in Figure 3-3(a) with L_C below 8 μm.

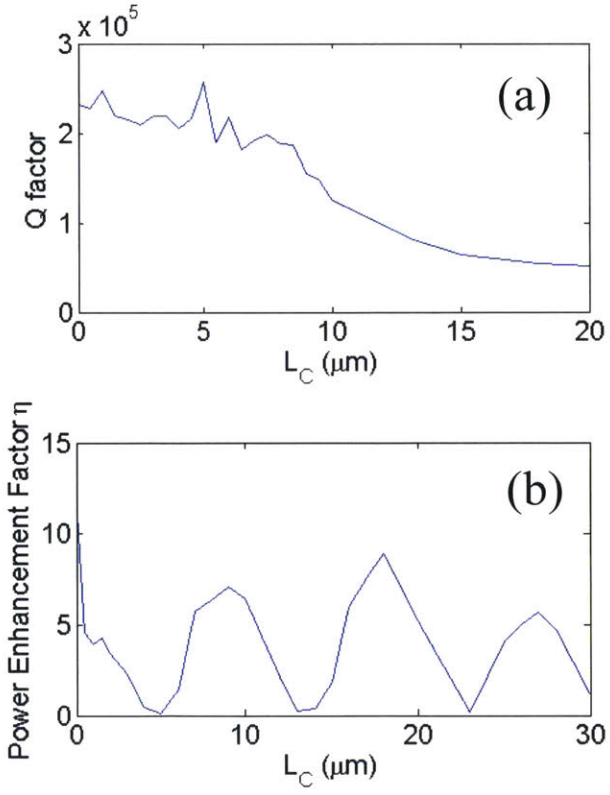

Figure 3-6 For a gap of 200 nm, (a) the cavity Q-factor at the signal wavelength (3.6 μm) changes with the coupling length, and (b) the power enhancement factor of the

6th-order mode at the pump wavelength (0.66 μm) changes periodically with the coupling length. An optimal coupling length L_C=8 μm is found.

On the other hand, the power enhancement at 0.66 μm varies periodically with L_C as shown in Figure 3-6(b), and even its peak value is much lower than those in Figure 3-5. The periodic trend occurs because the pump light goes back and forth between bus and ring waveguide at the coupling region, for large L_C. This causes a periodic change in coupling coefficient resulting in a periodic change of η. The low peak value is because the resonator at 0.66 μm becomes very under-coupled due to the increased gap. We find that, in the highly asymmetric coupler, the fundamental mode in the bus waveguide and the 6th-order mode in the cavity do not have their effective indices matched, which means that the light in the bus waveguide cannot completely transfer its power to the cavity mode [49]. Even the maximum coupling is still much less than the round-trip loss of the cavity mode at 0.66 μm, which is associated with a very under-coupled case. This can be confirmed by the fact that the lowest transmission values in the resonance spectra are 0.642, 0.626, and 0.665, corresponding to the η peak values at L_C=9, 18, and 27 μm, which are far away from a critical coupling case. A joint consideration of Fig. 6 reveals an optimal L_C of 8 μm with a Q-factor of 1.87×10^5 and η=6.34.

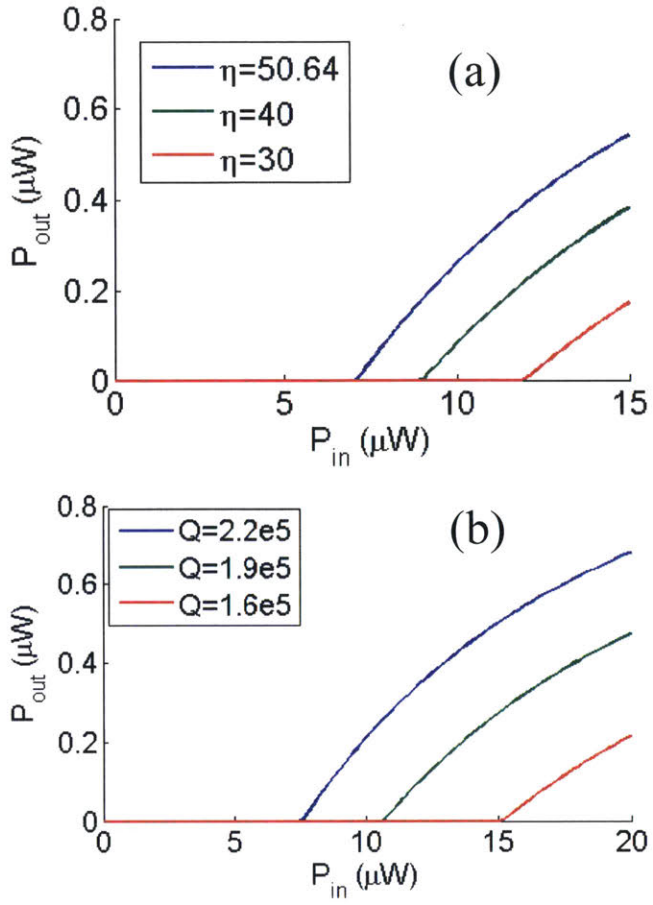

Figure 3-7 Lasing performance for gap=100 nm and L_C=0.6 μm, and accordingly the power enhancement factor η=50.64 at the pump wavelength and cavity Q=2.2×10^5 at the signal wavelength. (a) The influence of the power enhancement on the lasing threshold, (b) the influence of the cavity Q-factor is shown.

Then, by solving the rate equation at equilibrium condition, we obtain the laser performance curves in Figure 3-7. For a gap of 100 nm, the optimal operation parameters can be found at L_C=0.6 μm from Figs. 2.3 and 2.5, with η=50.64 and Q=2.2×10^5. Threshold power is 7.6 μW, and slope efficiency is 10.26%. As expected, the higher the

power enhancement factor, the lower the lasing threshold obtained, when we keep the Q factor the same at 3.6 μm, as shown in Fig. 7(a). Similarly, with an increased Q factor and η fixed at 50.64, less gain is needed to balance the loss, and threshold power also drops. For a gap of 200 nm, we choose L_C=8 μm, and the lasing threshold would be scaled with the power enhancement factor and increases to around 60 μW.

Chapter 4. Frequency Comb Generation

4.1. Dispersion engineering for comb generation

Instead of light emission from transitions between energy levels, which usually only provide limited linewidth, another potential approach to generate new frequencies is to use non-linear effects of materials. Optical frequency comb generation, which is based on microresonators and Kerr nonlinear effect, has attracted attention due to its potential applications in coherent communication, frequency metrology and optical signal processing [50].

To generate new frequencies in this kind of device, a stable soliton is generated in the microresonators. All the frequencies are at resonance and are enhanced by Four Wave Mixing (FWM). When they are mode-locked with each other, a stable soliton will be formed in the cavity, which transferred a CW pump source into a series of pulses.

To form the soliton, anomalous group delay dispersion is needed. Otherwise the front of the pulse will travel faster than the back of the pulse, which destroys the pulse and cannot form a soliton. To further compress the pulse and generate wider spectrum, flat dispersion curve which is close to zero is preferred. By tailoring nonlinearity and dispersion properties, broad band comb with bandwidth up to one octave can be achieved.

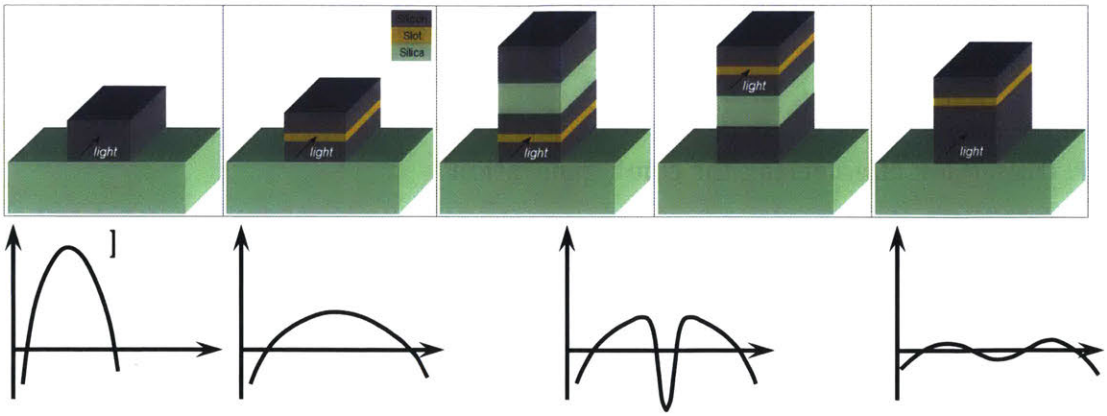

Figure 4-1 Dispersion engineering of waveguide[51].

As shown in Figure 4-1, strip waveguides have strong dispersion. Even at zero-dispersion wavelengths, the dispersion slope is large. By introducing a nano-scale slot produces a relatively flat and low dispersion. When the strip and slot waveguides are coupled, the transition from a strip mode to a slot mode occurs over a narrow bandwidth, causing highly negative dispersion.

Merging the two waveguides makes the negative dispersion smaller, which is used to flatten the overall dispersion profile in the strip/slot hybrid waveguide. The final result of the dispersion engineered waveguide is shown in Figure 4-2.

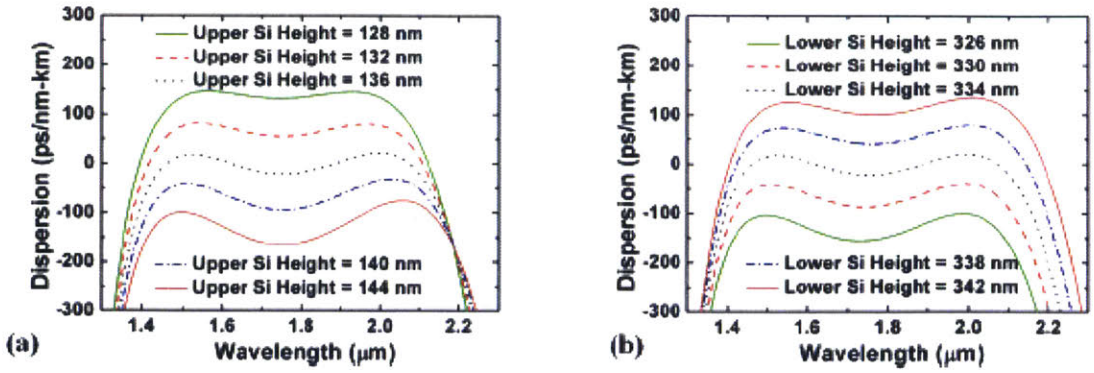

Figure 4-2 Dispersion is increased from normal to anomalous dispersion regime as (a) the upper height decreases or (b) the lower height increases, with a small change in dispersion slope[52].

However, there are several problems which need to be solved before fabrication of such a device. 1. The device is very sensitive to fabrication parameters. A change of height or width of 5 nm will result in a huge difference in dispersion. 2. The energy transfer efficiency drops significantly with increasing bandwidth. More precise tools are needed to measure the generated comb.

About the efficiency of energy transfer from pump to new frequencies, Bao etc. proved that this is limited by the bandwidth. In fact, under certain coupling condition, the product of bandwidth and efficiency is constant[50]:

$$N\eta = 0.09\,(F \cdot \theta)^2 = 3.53\,(over\ coupling) or\ 1\,(critical\ coupling)$$

Where N is the number of comb lines within the 3-dB comb bandwidth, η is the nonlinear conversion efficiency expressed as external pulse energy divided by the input energy, F is cavity finesse, θ is coupling coefficient.

From the equation we find that to increase the energy transfer efficiency, we can engineer the dispersion curve to the other extent: make it anomalous dispersion, but far away from zero dispersion. This will broaden the peak and generate less frequency lines, but provide much higher efficiency.

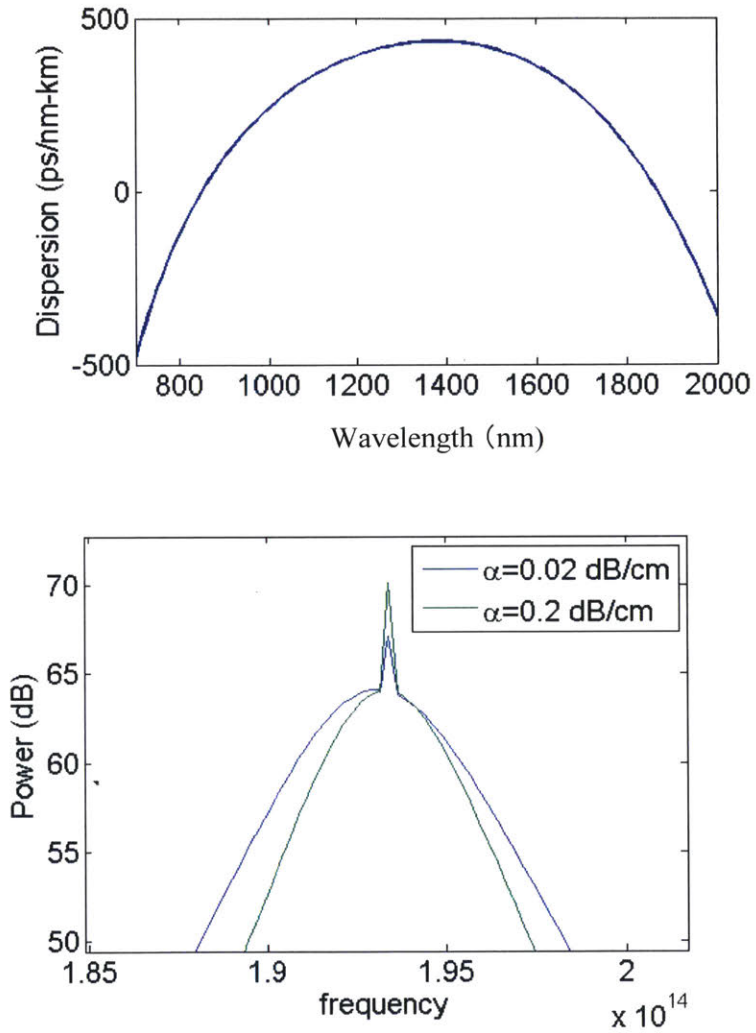

Figure 4-3 Waveguide dispersion and comb spectrum under difference cavity loss. The power unit is arbitrary.

As shown in Figure 4-3, this is the dispersion curve for 950 nm high 790 nm wide strip waveguide. The size of the ring resonator is the same as the straight waveguide. The substrate is 3 μm SiO_2 on Si wafer. Ring radius is around 100 μm and FSR is 0.25 THz. The input power is 100 mW. The waveguide cannot be too small, otherwise it cuts off quickly when wavelength increases. It cannot be too large also, otherwise material dispersion will dominate and become normal dispersion only.

If the loss is small (cavity loss α=0.02 dB/cm, Q~1×10^7), the 3dB band covers from 1536 nm to 1568 nm (4 THz bandwidth), with 15 comb lines in the band. The efficiency is around 23%. If the loss increases (cavity loss α=0.2 dB/cm, Q~1×10^6), the comb bandwidth narrows down to 3 THz and efficiency drops to 17%.

4.2. Thick LPCVD nitride growth and comb device fabrication

To grow high quality silicon nitride film, LPCVD tool is used to get stoichiometric film. This avoids hydrogen and extra silicon nano crystals in the film, both of which increase the loss in waveguides. However, LPCVD nitride will introduce high stress in the thin film. When grown on a 6-inch wafer for more than 300 nm, cracks will be generated. To avoid such cracks that travels across the entire thin film, trenches on silicon dioxide substrate are made prior to growth[53]. Instead of making trenches using diamond scribes, which introduce debris and is not CMOS compatible, we patterned the wafer by UV lithography and etched silicon dioxide layer as well as part of the substrate to define the trench. The structure of the wafer is shown in Figure 4-4. The substrate is 3 μm thermally grown silicon dioxide on silicon substrate. The depth of the trench is 5 μm in total. We etched through oxide layer to mimic the trench that the diamond scribe

defines. Trenches in oxide layer only cannot effectively stop the crack propagation[54].

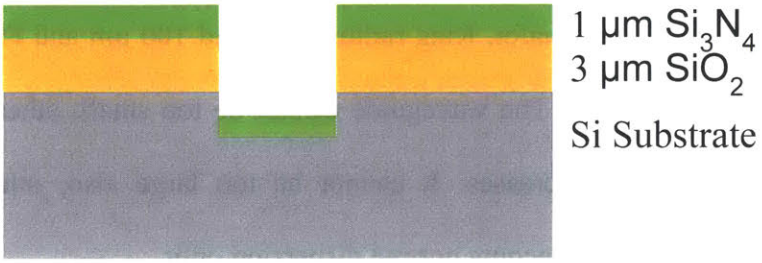

Figure 4-4 Structure of the LPCVD silicon nitride film with trenches

Such trenches define 2 cm by 2 cm square mesas, which will help release the stress. The trench also stops propagation of cracks when it is generated due to defects or while cleaving.

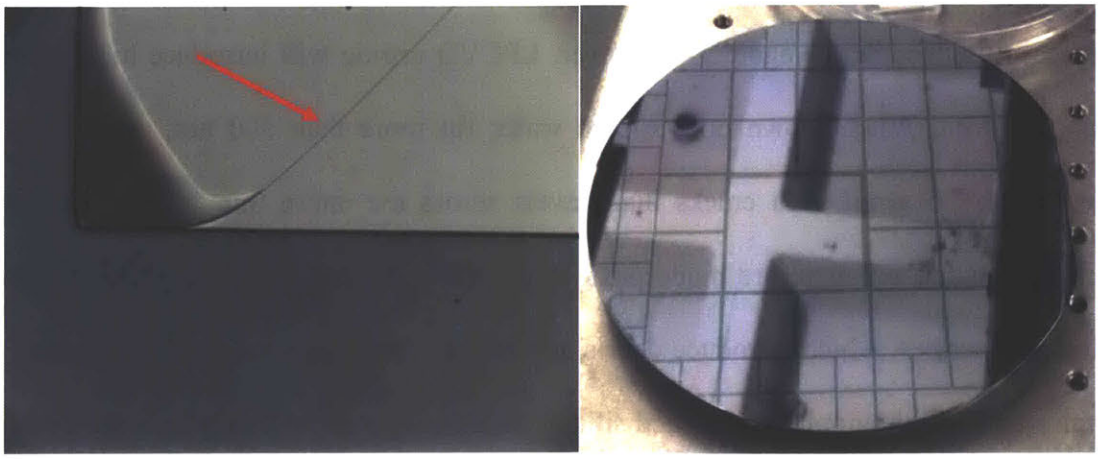

Figure 4-5 trenches on the wafer (right) and 10X microscope picture (left). The crack generated in one mesa stops at the trench boundary (pointed out by a red arrow).

As shown in Figure 4-5, the trench successfully stopped the propagation of cracks. Most of the 2 cm by 2 cm mesas are crack-free.

The silicon nitride wafer is then patterned by ebeam-lithography using 1.3 μm thick ZEP as photoresist. The exposure dose is 400 C/cm^2 and aperture is 240 μm. Then it is developed in ZED and rinsed by Methyl isobutyl ketone (MIBK) and Isopropyl alcohol (IPA). A gas mixture of 45 sccm CHF_3 and 15 sccm CF_4 with 200W RF power are used in a reactive ion etching chamber to etch the wafer. The wafer is then soaked in N-Methyl-2-pyrrolidone (NMP) to remove photoresist and then is cleaned in oxygen plasma and Piranha solution to remove the oganic residue. The final cross-sectional image is shown in Figure 4-6. The sidewall is vertical and smooth.

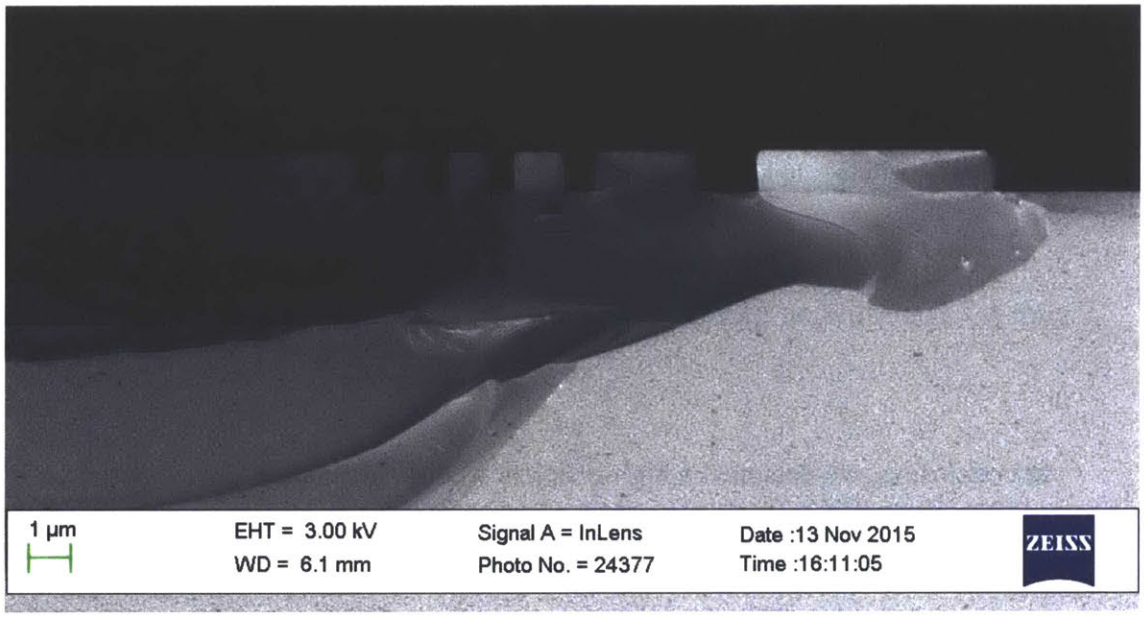

Figure 4-6 Cross-section image of silicon nitride waveguide structure.

The performance of the device is shown in Figure 4-7. It shows about 40 dB

extinction ratio at about 1562 nm. The Q factor is about 2×10^5, which is theoretically enough to generate the comb.

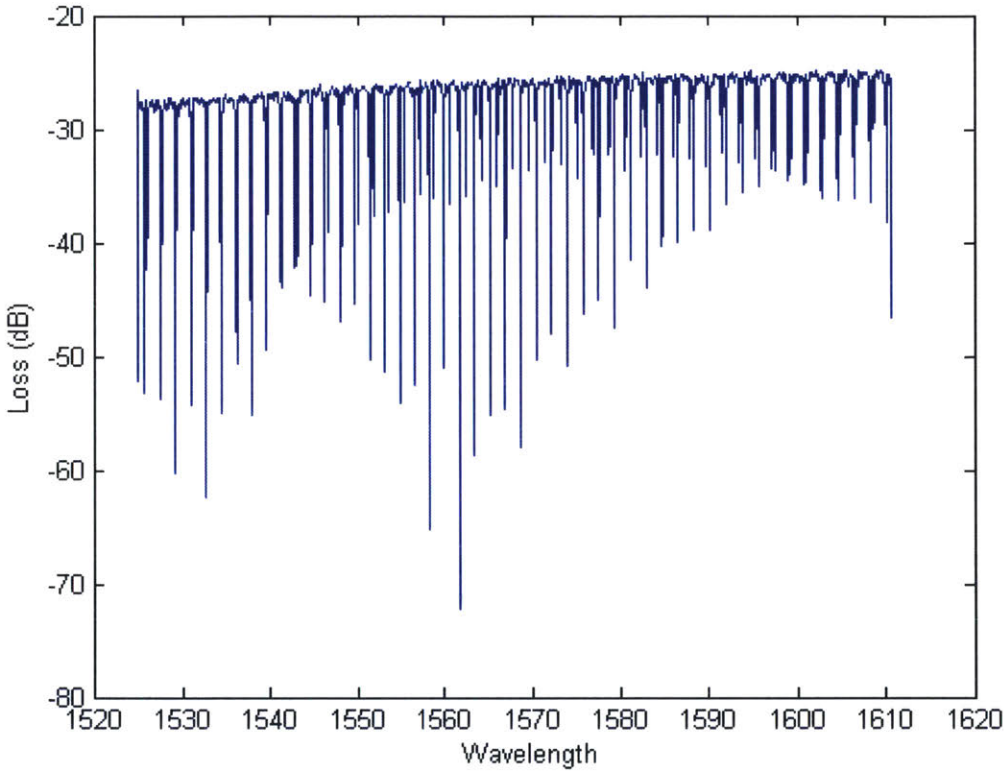

Figure 4-7 Transmission spectrum of the silicon nitride comb device.

In conclusion, we designed a high-efficiency comb generation device based on high-quality stoichiometric Si_3N_4 film. Trenches are made to release the stress and avoid propagation of cracks. The theoretical conversion efficiency can be up to 20%. A resonator device is fabricated and reaches a Q factor of 2×10^5.

Chapter 5. MIR Chalcogenide Glass Gas Sensor

5.1. Introduction

Analysis of the composition and concentration of chemical vapor mixtures is important in many fields including environmental monitoring[55], forensic analysis[56] and medical diagnoses[57]. The measurement of characteristic infrared absorption spectra has been widely used to gather such information. Traditional IR optical sensors use free-space geometry to measure transmission through a gas chamber. With the development of microphotonic fabrication technology, bulky free-space structures can be replaced by their on-chip counterparts enabling smaller footprints and reduced power consumption. Near-infrared (NIR) on-chip spectroscopy devices exist for various applications[58-64]. However, similar devices for the mid-infrared (MIR) regime (typically from 3 to 10 μm) are required because fundamental vibrational modes of most chemical bonds are located in this regime[1]. A number of material systems are currently being actively investigated for MIR sensing applications[65-71]. In particular, chalcogenide glasses (ChGs) have been proposed as attractive material candidates due to their wide transparency range (from visible to far infrared), low processing temperature and large capacity of compositional alloying [72].

In this chapter, we design and fabricate an on-chip chalcogenide glass mid-infrared gas sensor, whose performance is then quantified using methane-nitrogen gas mixtures.

5.2. Device fabrication and characterization

To fabricate the device, a 3 μm thick thermal oxide layer is grown on a silicon

substrate followed by spin-coating of a 1.8 μm thick photoresist (NR9) over the oxide and subsequent patterning using a Karl Suss MA4 Mask Aligner. A thick (1.2 μm) chalcogenide glass film ($Ge_{23}Sb_7S_{70}$) is deposited on the patterned substrate using a thermal evaporator (PVD Products, Inc.). The NR9 photoresist is lifted off in acetone and the sample is baked at 120 ℃ in a vacuum oven to remove moisture. The device characterization set-up is shown in Figure 1. The light source is a broadly tunable (2.5-3.8 μm, 5 nm linewidth) laser (Firefly, MSquared Laser Ltd.), which is coupled to a ZrF_4 MIR single mode fiber. Light from the fiber output is collected by an MIR camera for imaging and intensity measurements. Methane and nitrogen gas flows are controlled by individual mass flow controllers with a typical total flow rate of 3 sccm. After mixing, the gas mixture is delivered from the top of the sample into a polydimethylsiloxane (PDMS) chamber. The total pressure in the chamber is 1 atm and the measurement is conducted at room temperature.

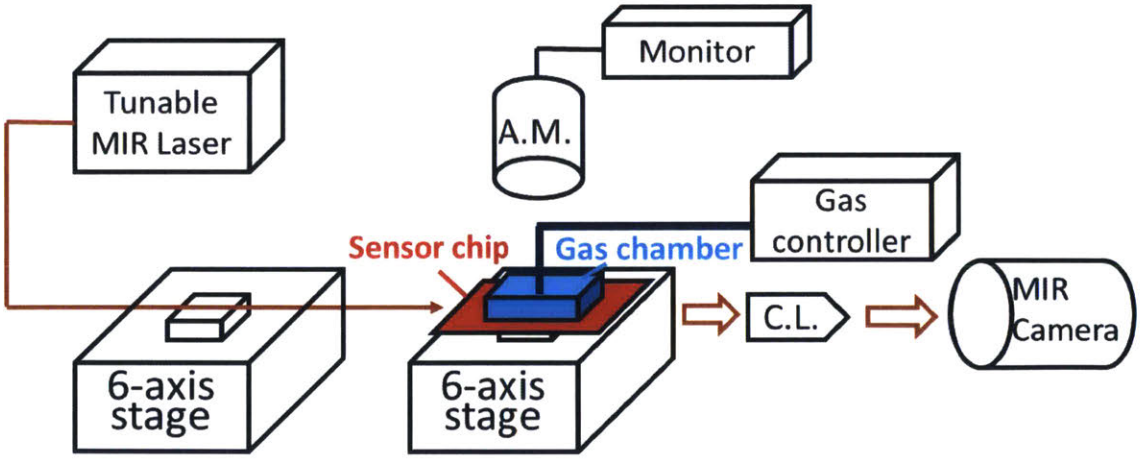

Figure 5-1. A schematic representation of the experimental set-up used to characterize the performance of fabricated MIR gas sensors. The probe light is coupled into the MIR fiber and then into the on-chip sensor (shown in red). The waveguide mode is captured by

the MIR Camera. A PDMS gas chamber (shown in blue) is built on top of the chip. A gas mixer and a flow controller mix N2 with CH4 and send the gas mixture to the chamber. Here, A. M. and C. L. represent alignment microscope and convex lens, respectively.

Our optical chip design includes a broadband spiral-waveguide sensor which significantly enhances the evanescent wave interaction length while maintaining a small device footprint, as shown in Figure 5-2.

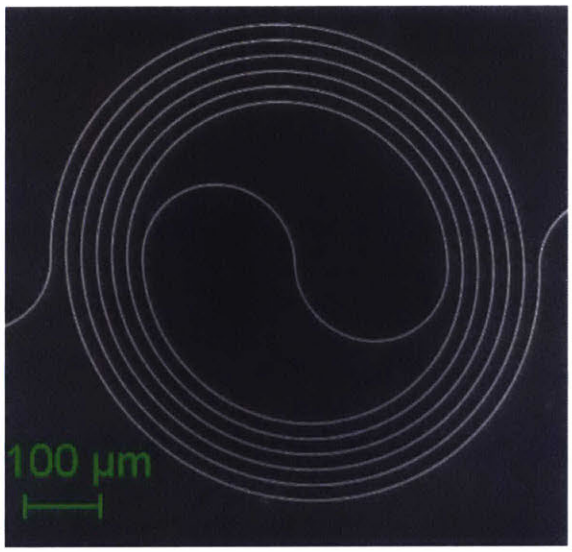

(a)

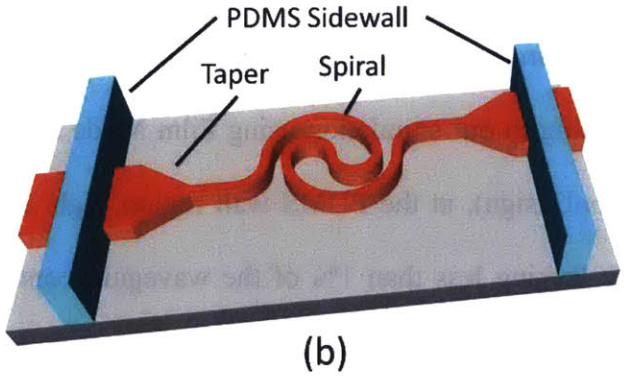

(b)

Figure 5-2. (a) Top view SEM image of a 2 μm wide single-mode spiral waveguide. The sensor chip contains spirals of different lengths. The left and right ends of the spirals connect to straight waveguide sections. Waveguide taper sections are inserted near the chip edges. (b) A schematic representation of the waveguide design. At the juncture where light crosses the PDMS gas chamber sidewall, the waveguide is 15 μm wide to better confine the light within the waveguide and decrease the absorption loss from PDMS. Within the chamber, the waveguide is tapered down to a single-mode width of 2 μm, to enhance evanescence which leads to enhanced gas-photon interaction.

The design and operation of the polymer gas chamber presents an unusual challenge due to the chosen MIR wavelength regime. The chamber is usually made of PDMS or other polymers for an air-tight seal. However, such polymers contain a large number of C-H bonds which absorb strongly in the MIR, especially near the absorption peak of methane gas. A direct exposure of the optical mode within the sensor to the PDMS chamber walls will dramatically decrease the transmission intensity and diminish the signal to noise ratio. To overcome this problem, we increase the waveguide width to 15 μm at the intersection of the waveguide and the PDMS wall region, and then taper the width down to 2 μm within the chamber to maintain single-mode operation, as shown in Figure 5-2(b). According to our simulation using Film Mode Matching (FMM) method (FIMMWAVE, PhotonDesign), at the PDMS wall region, light is well confined within the wider waveguide leaking less than 1% of the waveguide optical mode (evanescent field) to interact with PDMS. When the width goes back to 2 μm the evanescent field increases to 8%. This design increases the sensitivity of the device. The cross sectional image of the 2 μm × 1.2 μm waveguide in the chamber is shown in Figure 5-3.

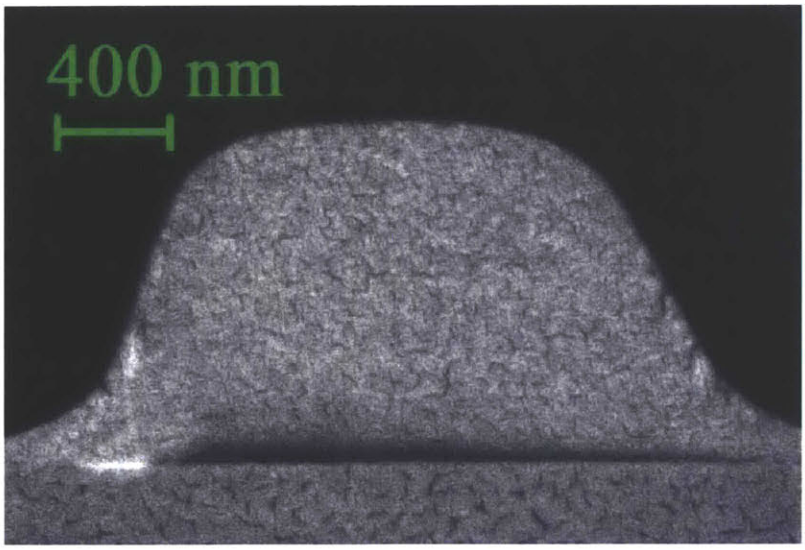

Figure 5-3. SEM cross-sectional image of the waveguide. The height is 1.2 μm and the width is about 2 μm. The "tail" at the bottom is due to photoresist undercut after lithography. Underneath the waveguide is 3 μm SiO2.

5.3. Methane sensing

The absorption spectrum of pure methane is measured through the waveguide, as shown in Figure 5-4. For this sensor, the total interaction length between light and gas mixture in the chamber is 2 cm (including the straight waveguide before and after the spiral parts which is around 1 cm long). The waveguide loss is around 7 dB/cm (mainly from the sidewall roughness) and the coupling loss is about 5 dB per facet. We measured the intensity at different wavelengths under nitrogen gas flow and use it as the baseline. Then we turn off N_2 gas and deliver 100% methane to the chamber. According to the Beer-Lambert Law,

$$T = \exp(-\alpha C \Gamma L) \qquad (5.1)$$

where T is the transmittance which is defined as the optical intensity transmitted through the waveguide immersed in the gas mixture normalized by the intensity with pure nitrogen gas. α is the absorption coefficient of 100% methane (partial pressure 1 atm). C is the volume concentration of methane. Γ is the confinement factor which indicates the overlap between the gas analyte and the optical mode (evanescent field). L is the total length of the waveguide. From Figure 4 we can find the absorption peak at 3310 nm. At 3310 nm the calculated absorbance per centimeter of methane calculated from the experimental data is 1.9, which matches the value from the NIST spectral database[73]. From the database of NIST, the absorbance at 3310 nm for 5 cm long path with 20% methane gas is about 1.6 (this equals to 1 cm long path with 100% methane). In a subsequent experiment with different methane concentrations, we choose to monitor the transmission change at 3310 nm, and the result is plotted in Figure 5. The data observed in Figure 5-5 agrees well with the transmittance for 100% methane (10-0.3), which is about a 3 dB loss and a transmittance of 50%.

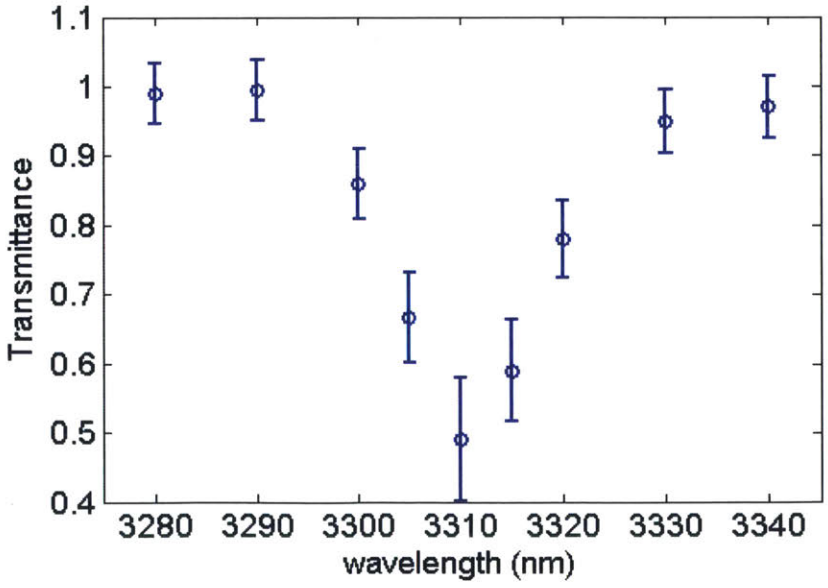

Figure 5-4. Transmission spectrum of 100% methane. The total flow rate of 3 sccm. Measurement is taken after the chamber reaches equilibrium. At 3310 nm it shows lowest transmission, which indicates the absorption peak of methane.

As expected, with increasing methane concentration, the transmittance decreases as shown in Figure 5-5. The error bar in the plot results from standard error of multiple measurements. The major source of the error is the laser power fluctuation. By (i) increasing the total length of the waveguide, or (ii) decreasing the width of the waveguide in the chamber, we can further improve the sensitivity of the device. With the same detection setup, the maximum effective length of the waveguide is around 4 cm before reaching the noise floor of the detector. The detection limit with current setup is around 2.5%. The major limits are the performance of the light source as well as the transmission loss of the waveguide. If the waveguide loss drops to 1 dB/cm (e.g. by using photoresist reflow or e-beam lithography patterning), the maximum effective length can be extended to about 30 cm and the detection limit will decrease to about 0.4%. In comparison, the free-space measurement with same light source, detector and footprint can reach a detection limit of 0.2%.

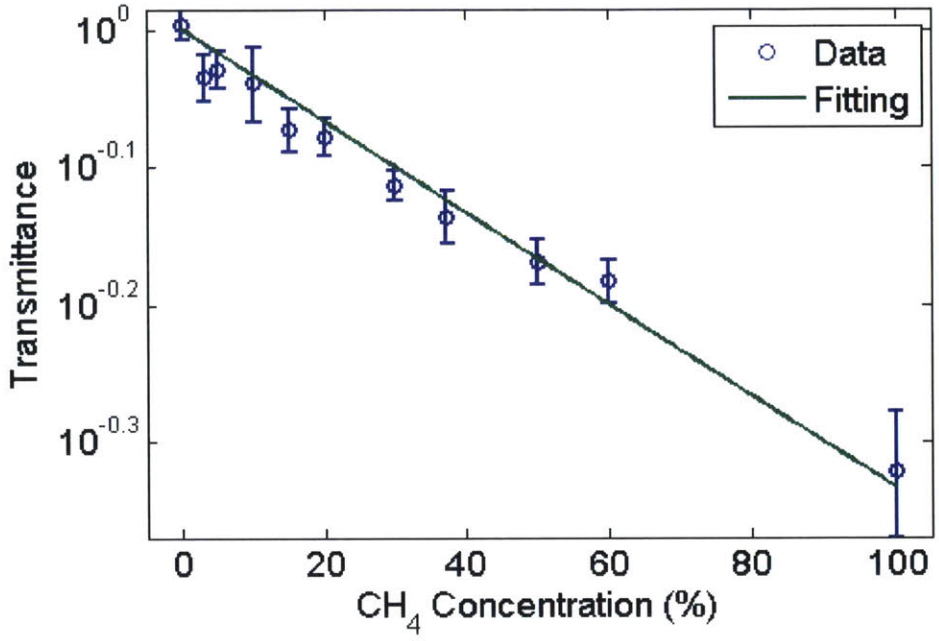

Figure 5-5. Transmittance with different methane concentrations. Y-axis is shown in log scale. The green line is the fitting curve following the definition of equation (5.1). At 3310 nm, optical transmission for different methane concentrations is measured, showing a responsivity of 0.77.

In conclusion, we demonstrate on-chip room-temperature MIR detection of methane/nitrogen gas compositions. We use a spiral-structure design to increase the interaction length and we use tapered waveguide structures to avoid high absorption loss at the intersection of the polymer chamber sidewall with the chalcogenide glass waveguide. The methane absorption peak at 3310 nm is used to quantify methane concentration in nitrogen down to 2.5 vol. %.

Chapter 6. Chalcogenide Plasmonic Phase Change Switch

6.1. Introduction

Photonic Integrated Circuits (PICs) have been considered as the critical technology for short reach communication systems, in which functional photonic devices with low power consumption and small footprint are highly desired[74]. Functional devices based on surface plasmonic polaritons (SPPs) have been proposed and studied to overcome the diffraction limit and increase the integration density, however, only few have addressed the active metallic nano-scale device. Generally, optical switches can be grouped by their working mechanism: optomechanical switches with low insertion loss and crosstalk, but slow switching speed (millisecond scale); electro-optic switches where the refractive index of the material in the coupling region of a directional coupler is varied by applying a voltage; semiconductor optical switches that employ ring resonators or Mach-Zehnder interferometers in which the refractive index of the optical path is changed by carrier injection mechanisms; switching achieved by thermo-optic effect, i.e. variation of the refractive index by changing the temperature, and other switches based on liquid crystals or acoustic effects. Recently, optical switches based on $Ge_2Sb_2Te_5$ (GST) chalcogenide glasses have been proposed [75] and demonstrated[76,77]. The optical properties of GSTs, i.e. refractive index and absorption, are changed by switching the material state between amorphous and crystalline, simply by applying a near band-gap optical field. Moreover, the index and absorption change remains in the material with no need of a continuous power supply, thus making these devices appealing for energy saving and optical memory applications. Ikuma et al. experimentally demonstrated an optically controlled

GST switch with a 9.7 dB extinction ratio between the amorphous and crystalline states in the wavelength range from 1525 to 1600 nm[77]. However, the control signal is applied through an external pulsed laser whose beam needs to be precisely aligned with the waveguide.

In this chapter, we propose a photonic ultra-subwavelength latch switch based on a metal-dielectric-metal waveguide structure integrated with $Ge_2Sb_2Te_5$ chalcogenide glasses. There are two important characteristics of GSTs that enable GST-assisted optical switches driven by electrical signals[78]. First, GST materials change their state from amorphous to crystalline by simple Joule heating [78]. Second, accurate spatial location control is obtained by lithographically patterned electrical contacts, hence alignment is embedded. Here we propose a structure which overcomes the two main challenges for electrically driven schemes: (i) metal contacts demonstrating low absorption, low resistance, and high temperature stability; (ii) low loss optical wave guiding with very thin (tens of nanometers) GST films. Our nanometer scale switch exhibits a high extinction ratio between ON and OFF states.

6.2. Chalcogenide Glass Plasmonic Phase Change Switch Design

The schematic of the proposed optical switch is shown in Figure 6-1. The GST is sandwiched by two gold thin films. Gold (i) enables the formation of an optical waveguide by Plasmon polaritonic resonance effect; and (ii) serves as an electrical contact. At the working wavelength of 1550 nm, the refractive index of GST is 4.4 + i0.098 for the amorphous state and 7.1 + i0.78 for the crystalline state6, while the refractive index of the gold is 0.55+ i11.51 [77]. The entire structure is surrounded laterally

by an electrical isolating SiO2 (refractive index 1.45) layer.

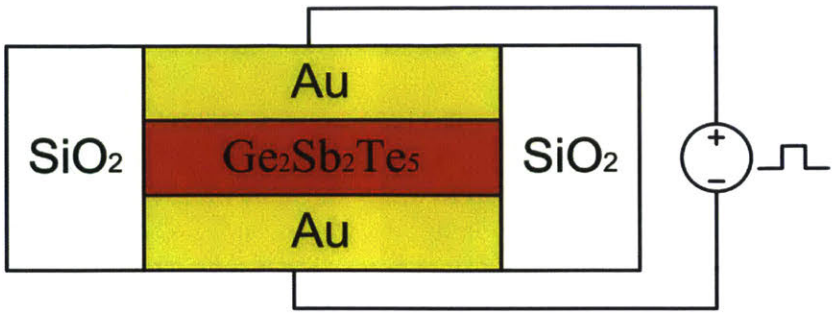

Figure 6-1 An electrically driven GST optical switch: the GST material is sandwiched by two gold thin films, and laterally surrounded by SiO2 for isolation. Gold (i) enables the formation of an optical waveguide by plasmon-polariton resonance effect; and (ii) serves as an electrical contact.

We use finite element method based multi-physics software to guide the analysis and design of the structure. In the simulations the following parameters are employed: a thickness of the GST layer of 50 nm, typical of electronic PCMs; a waveguide width of 30 nm; and thickness of the gold contacts of 100 nm. The electric field of the proposed structure is represented in Figure 6-2, which shows that the light is well confined in the waveguide due to the plasmonic resonance effect, and that the coupling between the GST and the metal is enhanced along the interface for the OFF states since the refractive index of GST in the crystalline state is larger than in the amorphous state.

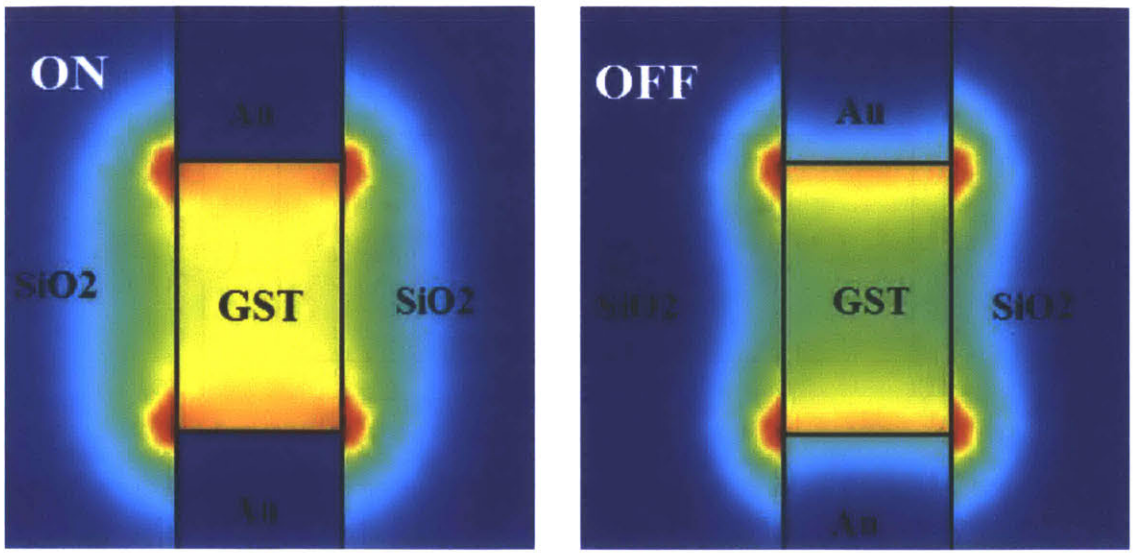

Figure 6-2 Simulated electric field of the GST-assisted plasmonic switch when the GST is in the ON state (amorphous) and OFF state (crystalline), assuming a waveguide core width of 30 nm and thickness of 50 nm. At 1550 nm refractive index of GST is 4.4 + i0.098 and 7.1 + i0.78 respectively for amorphous and crystalline states, while the refractive index of gold is 0.55+ i11.5. The effective indices are 4.184-i0.279 (ON) and 8.3359-i1.982 (OFF).

There are two important geometric parameters which affect the performance of the switch, namely, the width and the thickness of the GST film. We first investigate the impact of GST film thickness. Figure 6-3(a) represents the total insertion loss per unit of length of the switch as a function of the GST thickness from 10 to 50 nm (waveguide width is fixed to 30 nm). For both states the insertion loss of the switch decreases with thicker GST films. The OFF state (crystalline GST) always experiences a higher level of loss than the ON state (amorphous GST) because SPP resonance between GST and the gold layer is enhanced as GST film thickness decreases, thus inducing a higher

absorption loss.

Figure 6-3(b) shows the variation of insertion loss per unit of length of the switch as a function of the waveguide core width from 20 to 100 nm (the thickness of the GST layer is fixed to 50 nm). In general, losses vary differently with waveguide width in the ON (amorphous GST) and OFF (crystalline GST) states. In the ON state optical losses do not exhibit significant changes with waveguide width. However, in the OFF state higher width dependence is seen as higher losses are exhibited because (i) the mode leaks into the SiO2 layer and (ii) coupling with the lossy metal layer is stronger.

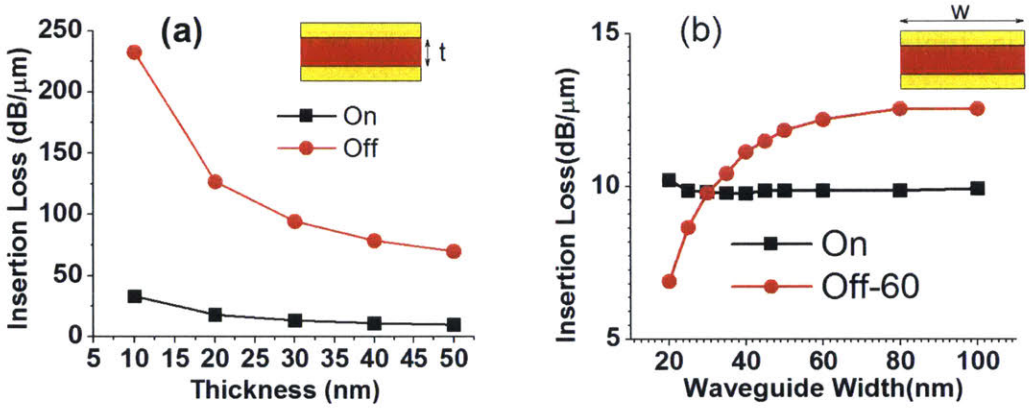

Figure 6-3 Insertion loss (IL) per unit of length of the switch as a function of the waveguide core parameters: (a) as a function of the GST thickness when the waveguide width is fixed to 30 nm (b) as a function of the waveguide width (WG width) when the GST thickness is fixed to 50 nm. Black solid lines and square markers indicate the ON state (amorphous GST), while red lines and circle markers refer to the OFF state (crystalline GST).

Figure 6-3(b) also shows that, the insertion loss for ON state changes slowly with the variation of waveguide width, while the insertion loss for OFF state is significantly increased with the waveguide width. This indicates that, a larger waveguide width will result in a higher extinction ratio between ON and OFF states. On the other hand, more energy is required to drive the phase change of the material. Therefore, there exists an optimum waveguide width if both between energy cost and extinction ratio are considered, as we will show below. It is noted that we choose the thickness of GST film as 50 nm, because 50 nm is a typical value used in PCM applications[77].

To find the energy cost and operation time of our switch structure, we build the Joule heat model that couples both electrical and thermal properties of the materials (listed in Table 6-1). We begin our analysis with the switching-off process, i.e. the transition of the GST material from the amorphous to crystalline state. The process is essentially a re-crystallization under high temperature, yet below the melting point of the material. The resistivity of amorphous GST is so high (typically about 10 $\Omega \cdot m$) that there is almost no measurable current below the threshold voltage. However, amorphous GST has a threshold voltage, occurring at a certain current density, above which it becomes conductive without any phase change, and consequently generates Joule heating that induces the phase change. The typical switching-off time (or "Set" process in PCM) of 100 ns is used[77]. This is much longer than the typical switching-on time (or "Reset" process), which is around 1 ns[79], which indicates that the energy consumption of the switching-off process is dominant, therefore requiring only an optimization of the energy cost for the switching-off process. The total energy cost is scaled by the length of the switch.

Table 6-1 Material parameters used in the electrical and thermal simulations

Material	**Conductivity ($\Omega^{-1}\cdot m^{-1}$)**	**Heat capacity ($J\cdot Kg^{-1}K^{-1}$)**	**Thermal conductivity ($W\cdot m^{-1}K^{-1}$)**
GST (crystalline)	2.77×10^{3} [80]	210 [81]	0.24 [82]
GST (amorphous)	0.1 [80]	210 [81]	0.28 [82]
GST (amorphous above threshold voltage)	2.77×10^{3} [80]	210 [81]	0.28 [82]
Au	4.52×10^{7} [83]	129 [83]	318 [83]

Figure 6-4 reports the power density and total energy of our switch. As shown in Figure 6-4(a), the electrical power density required for the heating process decreases with waveguide width because the effective surface increases, thus making the heat dissipation into substrate faster. However, the energy cost per unit of length of the switch required by the switching-off operation increases with the waveguide width because of the larger volume of GST. On the other hand, as shown previously, larger width also means larger extinction ratio per unit of length of the device.

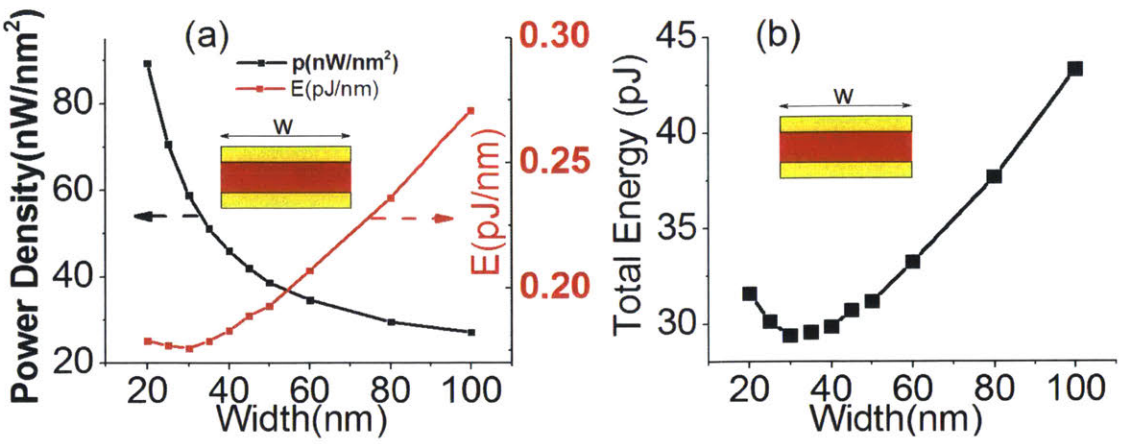

Figure 6-4 (a) Electrical power density (black solid line and square markers) and energy cost per unit of length (red solid line and square markers) required by the switching-off process as a function of the waveguide width (thickness is fixed to 50 nm); (b) total energy required by the switching-off operation as a function of the waveguide width, showing an optimal waveguide width of 30 nm.

Figure 6-4(b) instead reports the energy required for the switching-off process given a desired absorption change of 10 dB between the ON and OFF states. The optimal waveguide is 30 nm (width) × 50 nm (thickness) × 167 nm (length), which gives an insertion loss of 1.64 (On) and 11.64 dB (Off), with operation energy of only 30 pJ.

For the switching-on process, the crystalline GST melts into liquid and then is rapidly quenched, typically within a few nanoseconds[84], which results in an amorphization of the structure[79]. Assuming that the conductivity of the crystalline GST does not change before melting, and applying a voltage of 3.5 V [84], we calculate a current density of 1.94×10^4 kA/cm2. After 57 ps, the maximum temperature reaches the melting temperature (883K[80]). With further heating, GST will melt and the latent heat (1.37×10^5

J/kg) will consume most of the input power, pinning the temperature to the melting point. By treating the conductivity of GST as constant and assuming that all the heating energy goes into latent heat after 57 ps, the total phase transition time is only 0.12 ns, which is a little shorter than other reports[79]. The energy consumption required for the phase transition is 0.4 pJ, which is much smaller than that of the switching-off process. So the energy consumption per cycle (including both the switching-on and switching-off processes) is 30.4 pJ.

In conclusion, we propose an electrically driven plasmonic optical latch switch integrated with Ge2Sb2Te5 chalcogenide glass. The switch is characterized by a nanometer scale size and a high extinction ratio. For a 167 nm long switch, the total energy required is 30 pJ for switching-off and 0.4 pJ for switching-on processes, while the extinction ratio between amorphous and crystalline states is 10 dB at the wavelength of 1550 nm.

Chapter 7. MIR Integrated PbTe Detector

7.1. Introduction

Detection of infrared radiation is key to many technical applications including night vision[85], chemical sensing[86,87] and medical diagnostics[57]. Traditional IR photodetectors assume free-space geometry. Recently, miniaturization enabled by microphotonic fabrication technology has led to the development of waveguide-integrated photodetectors. Compared to their free-space counterparts, waveguide integrated devices typically decouple the optical absorption path from carrier transit path, which reduces response time in the case of photovoltaic detectors and enhances gain in the case of photoconductive detectors. The small active volume of waveguide-integrated detectors also improves the signal-to-noise ratio by suppressing the generation-recombination noise. Waveguide-integrated detectors based on Ge[88] and III-V materials[89] have been demonstrated in the near-IR telecommunication bands and their performance advantages have been well established. Although waveguide-integrated mid-infrared detectors are essential components for mid-infrared (MIR) system-on-a-chip platforms such as spectroscopic sensors[90], they are much less explored due to the limited material choices. III-V materials and HgCdTe widely used in free-space MIR detectors[85] require epitaxial growth on a lattice-matched substrate and therefore integration on silicon often resorts to a hybrid bonding approach: for example, integration of GaInAsSb detectors on silicon waveguides was demonstrated via adhesive bonding[91,92].

Lead chalcogenides represent a promising alternative material system for MIR

detection[93,94]. In particular, polycrystalline PbTe can be deposited by thermal evaporation directly on a variety of substrates including silicon and has been explored as a candidate for a low-cost silicon-integrated MIR detector solution[95-97]. In addition, our prior work shows that fast oxygen diffusion along the grain boundaries enhances optical response of the PbTe material by creating spatial charge separation and thereby increasing the carrier lifetime[97,98]. In this section, we demonstrate a waveguide-integrated PbTe detector monolithically integrated on a silicon substrate and operating at room temperature.

7.2. PbTe sample design and preparation

The device uses a 4" silicon wafer with a 3 μm thick thermal oxide layer as the starting substrate. All the thin films for device fabrication (PbTe, Sn and $Ge_{23}Sb_7S_{70}$ glass) are deposited by thermal evaporation used in previously reported protocols[98,99]. A PbTe layer is deposited first, followed by a 300 nm thick Sn contact layer with the $Ge_{23}Sb_7S_{70}$ (GeSbS) waveguide layer on top. We choose $Ge_{23}Sb_7S_{70}$ chalcogenide glass as the waveguide material given its superior chemical stability and compatibility with PbTe materials[72].

Two sample layouts are used to examine the performance of PbTe detectors: (1) A free space sample consisting of a 650 nm thick PbTe layer with Sn contacts of 0.5 mm spacing patterned using a shadow mask and without the glass waveguide layer. It is used to characterize the material property of PbTe. (2) An integrated sample, with a 100 nm thick and 40 μm long PbTe layer, followed by Sn contacts with 7 μm spacing and an 800 nm thick single-mode GeSbS waveguide on top. The integrated sample is patterned by a

lift-off process[99]. The cross-section schematic of the integrated device is shown in Figure 7-1(a).

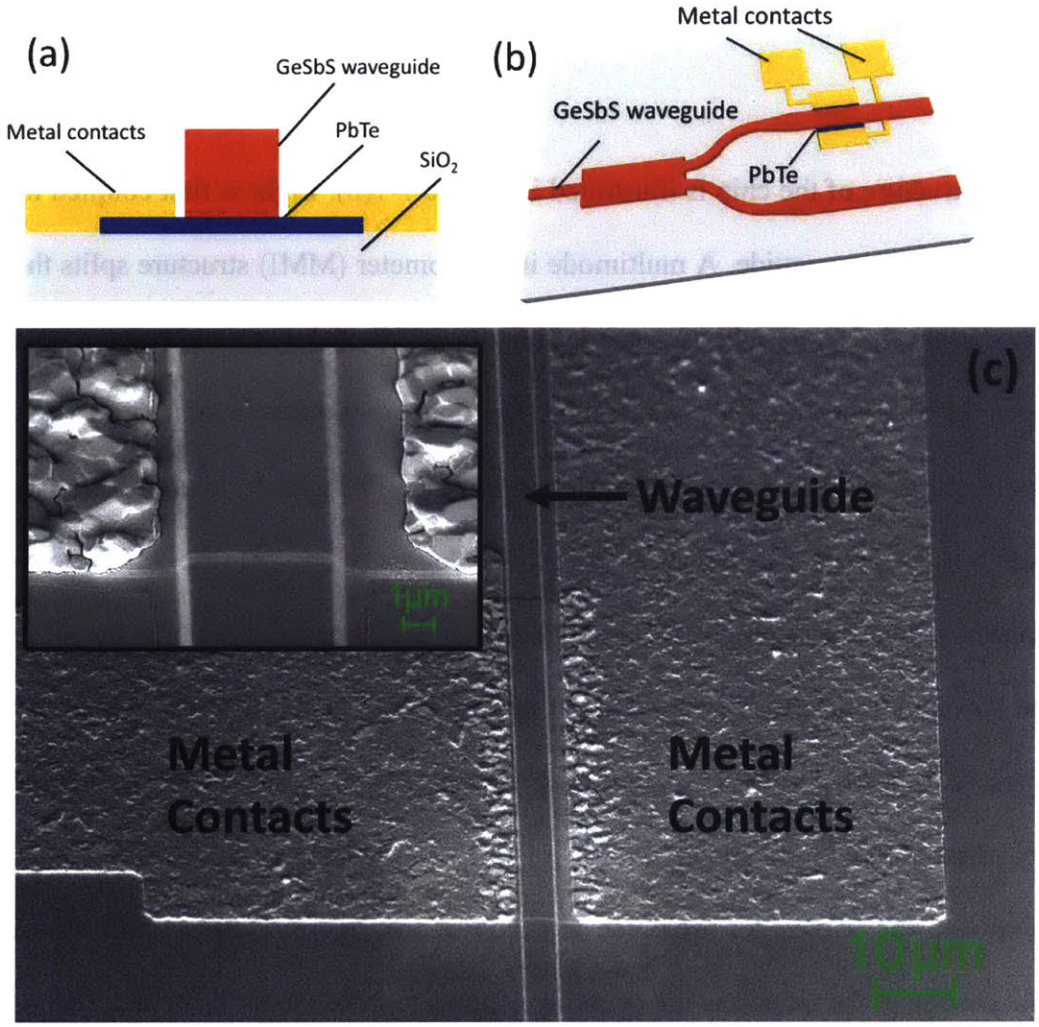

Figure 7-1. (a) A schematic cross-sectional view of the integrated MIR detector (not to scale). The thickness of the PbTe layer is 100 nm (blue region) and the width is 13 μm. The width of the waveguide is 5 μm and the height is 800 nm. Metal contact spacing is 7 μm, which means that they are 1 μm away from the waveguide. Underneath the waveguide is 3 μm SiO2. (b) A schematic representation of the chip design. An MMI structure splits the light into two arms. The lower arm is used for alignment. The upper

arm delivers light to the PbTe detector (blue region). Both arms adiabatically increase in width from 2 μm to 5 μm. The PbTe layer and Sn contacts lie underneath the waveguide. (c) A 45-degree view SEM image of the MIR device.

The structure of the chip is illustrated in Figure 7-1(b). Light is first coupled into a 2 μm wide GeSbS waveguide. A multimode interferometer (MMI) structure splits the light into two arms that gradually increase to a 5 μm width to improve alignment tolerance between the PbTe layer and the waveguide. The upper arm delivers light into PbTe where most of light is absorbed. The lower arm, without the PbTe layer, is used for alignment. Figure 7-1(c) shows the SEM image at 45-degree view. At the interface of the detector/non-detector section, a clear boundary can be observed due to the abrupt change of the waveguide height. To evaluate the device design at the detector section, we use Film Mode Matching (FMM) method in FIMMWAVE (PhotonDesign) to simulate the mode propagation[100], as shown in Figure 7-2. TM-polarized light from the laser is coupled into the waveguide from the left side of the figure. Despite the cross-section profile change at the interface, the coupling efficiency from the fundamental TM mode in the glass waveguide to the hybrid TM mode at the detector section is 94% with only about 4% reflections. Coupling into the PbTe strip-loaded mode is minimal (< 1%) due to the large effective index and modal profile mismatch. Parasitic absorption by the Sn contacts is less than 0.1% according to the simulation. The decay length of the hybrid mode in the detector section is 16.7 μm.

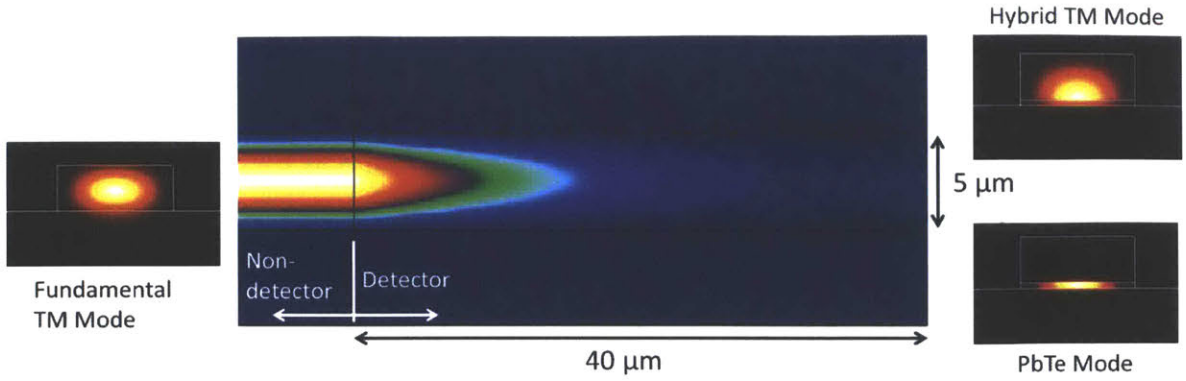

Figure 7-2. Simulation results of mode propagation in the PbTe detector (top view). Coupling efficiency from the fundamental TM mode at the non-detector section (mode shape is shown on the left) into the hybrid TM mode at the detector section (shown on the top right) is 94%. Totally less than 1% of the power is coupled into the PbTe mode (example shown on bottom right). The absorption length in the detector section is 16.7 μm.

7.3. PbTe thin film quality

Sample 1 is used to characterize the quality of the PbTe thin film. The key of making high-quality PbTe film with better signal to noise ratio, is to increase the resistivity thus decrease the dark current. Thermal evaporated PbTe film is usually n-type due to the Te-deficient nature. Extra oxygen introduced in the thin film will form PbO^{+} electron traps and switch the material into p-type. By this compensation of carriers, the resistivity can significantly decrease.

In previous experiment we did oxygen sensitization by oxidation outside the chamber. Continuing the work from previous student, we increased pressure of the

evaporation chamber to oxidize the thin film while doing the deposition. The pressure goes from 1×10^{-6} torr to 1×10^{-4} torr. The key properties are shown in Table 7-1 below. All samples are p-type.

Table 7-1 Material property of PbTe thin film from Hall Effect Measurement

Samples	**Carrier density (cm^{-3})**	**Mobility ($cm^2/V\cdot s$)**
120 nm PbTe, 1×10^{-6} torr	4.80E+16	8
250 nm PbTe, 1×10^{-6} torr	1.45E+15	53
150 nm PbTe, 1×10^{-4} torr	1.17E+15	35
630 nm PbTe, 1×10^{-4} torr	9.20E+14	32

From the table, it's obvious that we get less carrier density in the thin film deposited in higher chamber pressure.

Sample 1 is sealed in an IR-transparent glass chamber with a thermoelectric cooler (TEC) and a responsivity measurement is subsequently performed at -60 °C. IR light from a white light source passes through a monochromator and directly illuminates the chip. The contacts are wire-bonded to a source measurement unit to obtain the I-V curve of the device at different wavelengths. Data is gathered at -60 ° C to decrease the dark current (since the optical power from the monochromator is much weaker than the laser

used for sample 2, we need to decrease the dark current to improve the signal to noise ratio).

The wavelength-dependent responsivity of sample 1 under 10 V bias is shown in Figure 7-3. We measure the photoconductivity signal in the wavelength range of 0.8–5 μm in the PbTe film. This is consistent with our prior measurement results[97]

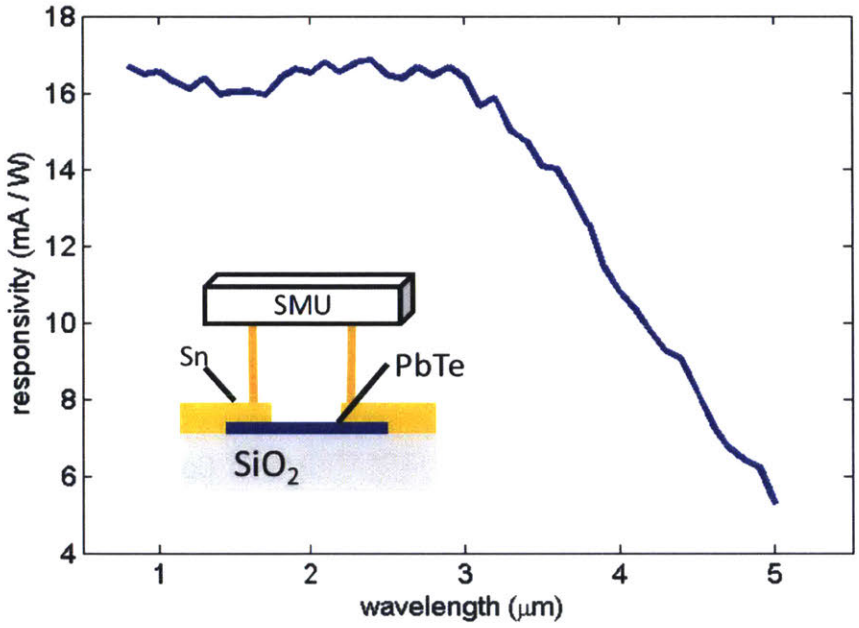

Figure 7-3 Response of sample 1 at different wavelengths at 213 K (-60 °C). The bias is 10 V. The spacing between contacts is 0.5 mm. The response drops after 3 μm as the photon energy is close to the band gap of PbTe. The inset is a schematic of sample 1. Sn contacts are wire bonded to a source measurement unit (SMU) to measure the I-V curve.

7.4. Integrated PbTe detector performance

For the integrated sample (sample 2), PbTe absorption measurement is performed at

room temperature using a device characterization set-up as shown in Figure 7-4. A tunable Cr2+:ZnS/Se laser (2.0-2.5 μm, IPG Photonics) is first coupled to an aspheric lens (C037TME-D, Thorlabs) and then focused into the waveguide. Light from the waveguide output is collected by an IR camera for imaging as well as intensity measurement in the alignment arm. A source measurement unit (Keithley 2401 SMU) is connected to the metal contacts on the chip via two probes to measure the I-V curves.

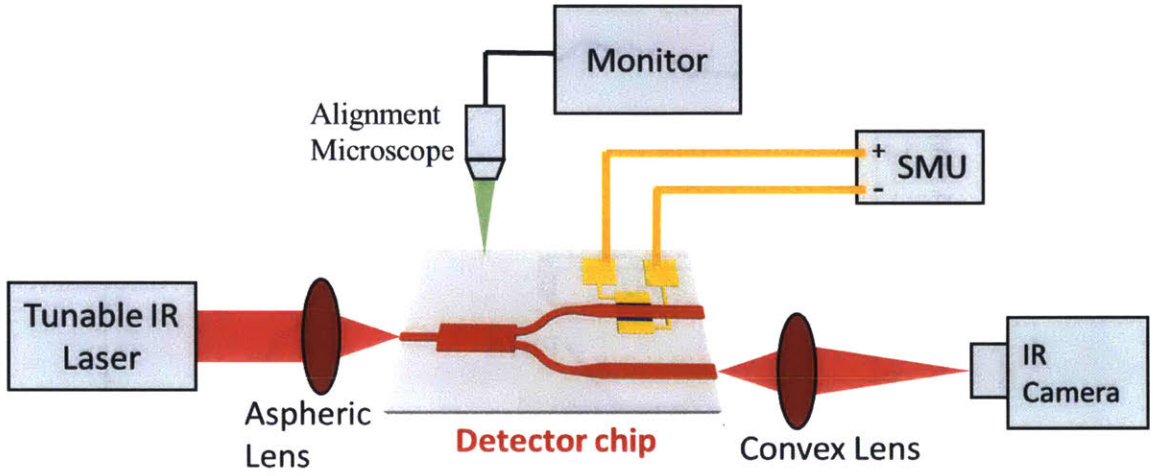

Figure 7-4. A schematic representation of the experimental set-up used to characterize the performance of PbTe detectors.

Sample 2 is measured at room temperature. Optical power coupled into the detector is estimated by subtracting the power loss due to fiber/lens coupling from the total input laser power. Based on the data shown in Figure 7-5, we calculated the responsivity to be 1.0 A/W at 2250 nm wavelength. Wavelength-dependent responsivity from 2.1 μm to 2.5 μm wavelengths is plotted in Figure 6. Within our measurement error, the responsivity remains roughly constant throughout this range, which is consistent with the trend shown in Figure 7-3.

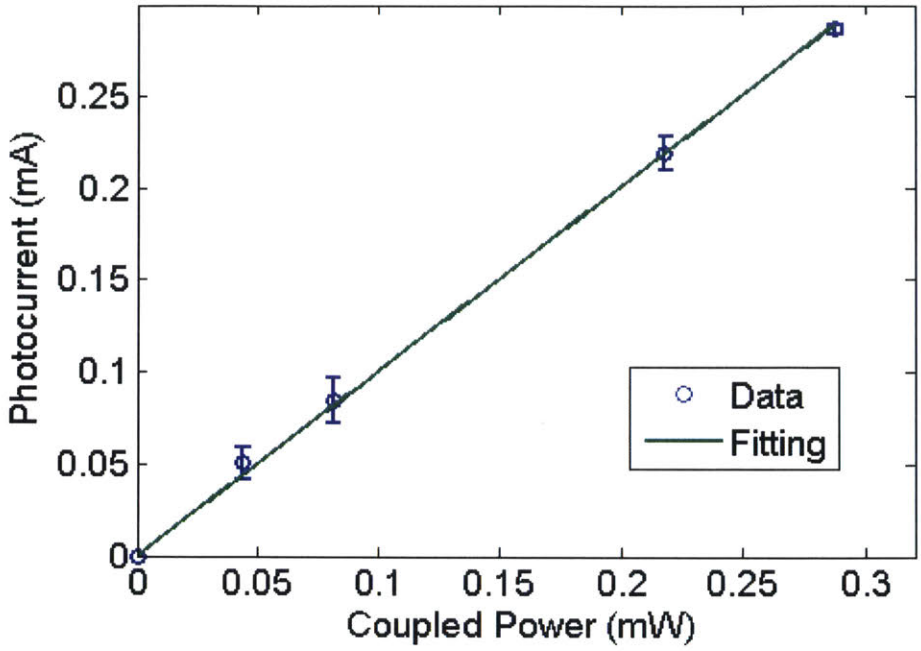

Figure 7-5. Photocurrent change as a function of optical power for the integrated device at room temperature and a fixed wavelength of 2250 nm under a bias of 10 V. Responsivity calculated from curve fitting is 1.0 A/W.

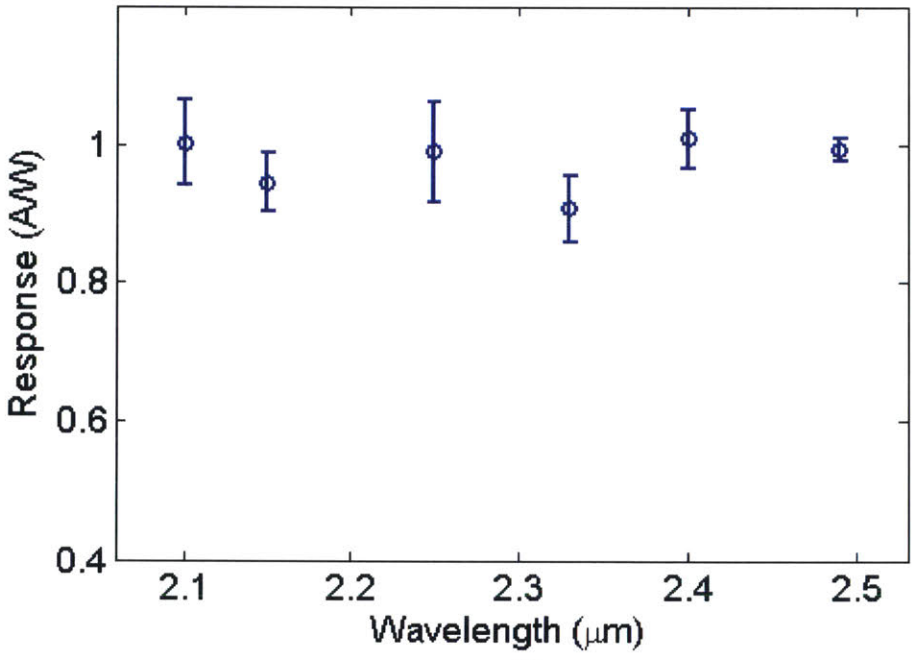

Figure 7-6. Uniform responsivity of the integrated detector as a function of wavelength (room temperature)

The error bars associated with the data shown in Figure 7-5 and Figure 7-6 are due to misalignment caused by mechanical vibration of the sample stage. Resistivity of sample 2 (dark) is 1.27 Ω-cm. The theoretical responsivity at 2.25 μm, assuming unity absorption efficiency and unity photoconductive gain, is about 1.8 A/W. Our device therefore exhibits a photoconductive gain of 0.59 taking into account the simulated 94% optical absorption efficiency. This figure is consistent with the carrier lifetime and transit time estimated based on the device geometry and Hall carrier mobility. The Johnson noise spectral density calculated from the dark resistance of our device is 8.6×10^{-13} $A/Hz^{1/2}$, which is much larger than the generation-recombination noise (about 1×10^{-19} $A/Hz^{1/2}$ based on Hall Effect measurements). Since current flowing through a photoconductor does not have shot noise[101], Johnson noise limited detectivity of this device is therefore 2×10^{12} cm-$Hz^{1/2}$/W.

The results above demonstrate the viability of using polycrystalline PbTe materials for on-chip integrated MIR detection. Further improvement can be made by (1) cooling down the system to decrease the Johnson noise which limits our SNR; (2) using an optical coupler to improve the coupling efficiency to PbTe; and (3) alloy PbTe with SnTe (band gap ~ 0.19 eV) to create smaller band gap materials and extend the detection range[102].

In conclusion, we demonstrate the first room-temperature MIR waveguide-integrated

PbTe photodetector. The responsivity is about 1.0 A/W at the 2.1 to 2.5 μm MIR regime. This platform provides a promising low-cost planar detector solution for MIR lab-on-a-chip devices.

Chapter 8. Future directions

8.1. Pocket-size toxic gas sensors

With the designs and devices shown in previous chapters, we now have solutions for an integrated MIR gas sensor. We have demonstrated the first (i) MIR methane sensor using a chalcogenide glass waveguide, and (ii) PbTe MIR detector integrated with a chalcogenide glass waveguide, which works even at room temperature. With these two major monolithically integrated breakthroughs, we have successfully demonstrated a path forward to shrinking the large free-space MIR spectrum analyzer to the chip-scale.

We can envision building our photonic sensor monolithically on top of the data collection and data processing logic circuits fabricated in the silicon platform beneath. The information collected from the sensor can be processed directly by the CPU and sent to an application interface, e.g. mobile phone apps. One can then check for toxic gases or air pollution in real time and everywhere. Besides, if dangerous chemical vapors (e.g. carbon monoxide) are detected, the sensor can send out warning signals ahead of time to avert tragedies.

The advances in the integrated MIR sensing also enable vastly connected sensor networks which offer high sensitivity and specificity. The fabrication cost as well as the energy consumption of each sensor will go down. This paves the way to the "Internet of Things" which needs multiple sensors to form a network. The information collected by the sensors will be shared among related things (e.g. apartment, bus, ship, police office) to better serve the people.

By integrating the sensor with a communication chip, we can simultaneously send information about the condition of the air to a lager national or global network, thereby building a distribution map of different gases. With this map, we can study the evolution of air pollution and/or discover dangerous chemical leakage.

In the following sections, I will talk about some specific future improvements we can make from the material and device design point of view.

8.2. Chalcogenide glasses and Ge for nonlinear photonics

Other than Si_3N_4, Ge and Chalcogenide glasses are also great candidates for integrated nonlinear photonics applications, especially in the mid-infrared regime, due to their relatively high nonlinear coefficient and low absorption. With this new material platform, broader band frequency combs can be generated in the MIR (3-6 microns) to be used as light sources for molecular finger-printing in the longer wavelength range (6-12 microns).

Specifically, chalcogenide glasses, can be reflowed to obtain smooth waveguide sidewalls which yield a high Q-factor[103]. With an appropriate design, the dispersion can be flattened and a wide frequency comb can be generated[51]. To improve the performance and demonstrate comb generation, the following specific directions can be considered in the future.

1) Improve thermal conductivity and optical damage threshold

Unlike silicon nitride whose melting point is above 1800 °C, and which can be heated up to 1000 °C without damage (annealing temperature used to remove hydrogen), the glass transition temperature of the common chalcogenide glass is relatively low. The photo-induced damage at high pumping level (which is necessary for nonlinear application) may shift the resonance peaks or even melt and break the device[104].

To solve this problem, we can (i) develop robust chalcogenide glasses, (ii) improve design (waveguide dispersion engineering) to decrease the threshold power required for nonlinear applications, or (iii) saturate device under long-time exposure to light (laser beam or lamp) to at least stabilize refractive index changes during operation.

2) Improve etch recipe

Ahigh Q-factor can be obtained by combining e-beam lithography and reactive ion

etching for GeSbS glass, the current recipe using fluorine results in a fluoride polymer residue on the waveguide. These polymers are hard to remove due to the chemical stability of the C-F bond. An extended soak in N-Methyl-2-pyrrolidone (NMP) along with sonication and oxygen plasma cleaning can remove most of the polymer, but not all. This thin layer of polymer does not have a high absorption coefficient in the near-IR regime. However, it is lossy at mid-IR wavelengths due to the absorption of the C-H bond. The SEM image of the waveguide after etching and before plasma cleaning is shown in Figure 8-1. The top layer has a "bunny ear" structure (pointed out by red arrows on top of the waveguide) which is the fluoride polymer leftover along the edges. The random grass-like structure on the sides is due to the micro-masking effects of the sputtered fluoride polymer and can be reduced by using lower pressure while etching.

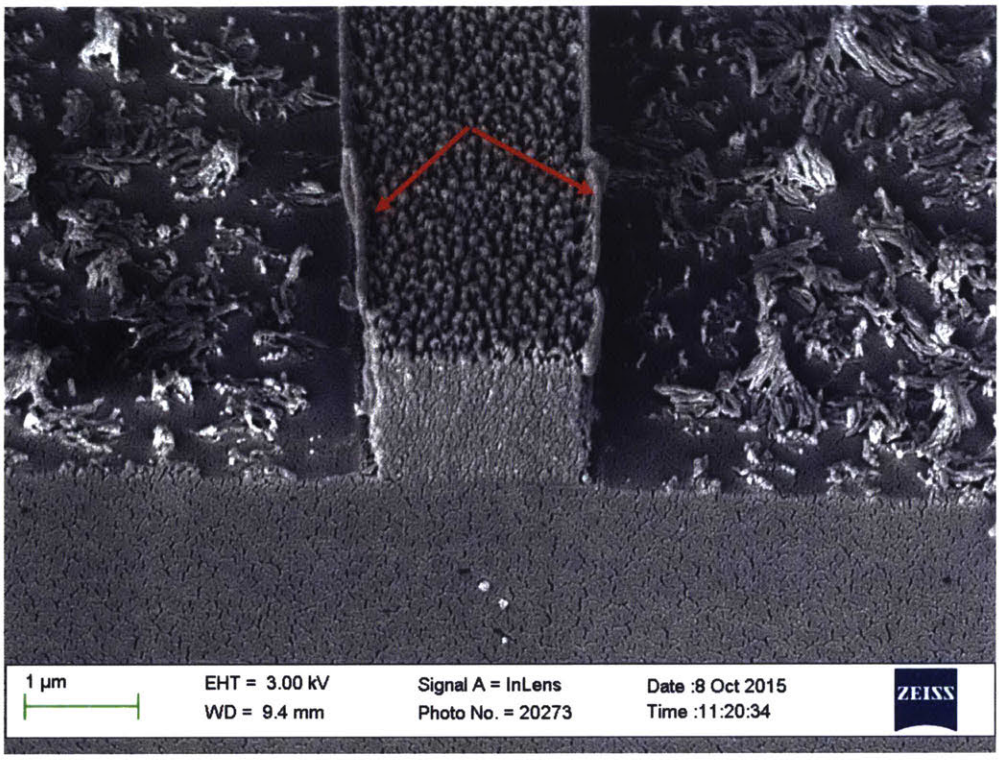

Figure 8-1 the 45-degree view SEM image of the GeSbS waveguide after fluoride etching and NMP cleaning before oxygen plasma treatment.

Fluoride polymer residues on silicon nitride waveguides can be cleaned with a

Piranha solution. However, chalcogenide glasses are not strong enough for Piranha solutions which destroy the device. Adding oxygen into the etching gas mixture can remove the fluoride polymer, but results in non-straight sidewalls due to the absence of protection by the polymers during etch.

To avoid the etching residue, lift-off is still one of the best candidates for patterning. Double-layer liftoff using ZEP photoresist as top layer and Poly(methyl glutarimide) (PMGI) underneath can provide both smooth sidewall (due to e-beam lithography on ZEP) as well as enough undercut (due to the isotropic dissolution of PMGI while developing ZEP). Other technology such as using a metal mask instead of an organic polymer may also work. The schematic of the process is shown in Figure 8-2.

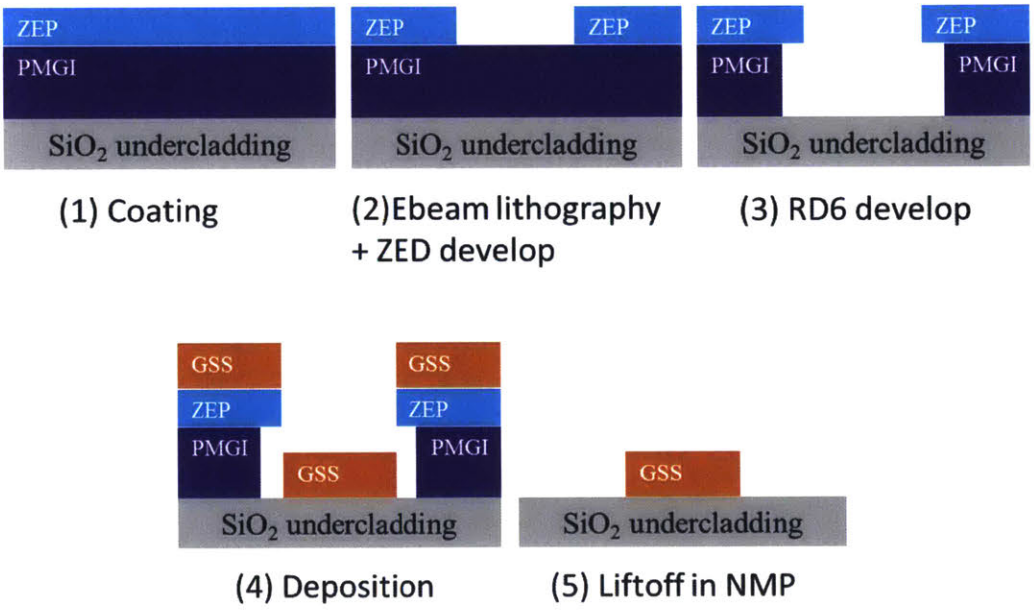

Figure 8-2 Schematic of the double-layer lift off process.

3) Ge as an alternative nonlinear material

Ge has a refractive index higher than that of Si, a better thermal stability than chalcogenide glasses, and Si-CMOS compatibility because it can be grown epitaxially on a Si substrate.

Ge can be etched by many common reactive gases including CHF_3, CF_4, SF_6 and Cl_2[105-107]. The chlorine gas etching is "clean" without polymer residues. However, without the protection layer, the sidewall of Ge waveguide after chlorine etch is rough. If a fluoride gas is used it can protect the sidewall of the waveguide but the polymer residue-removal problem remains (as for chalcogenide glasses). Unlike Si which can be protected by a native SiO_2 layer, GeO is not chemically stable and can dissolve in water, so we cannot use a Piranha solution to remove the polymer residue. Since Ge is epitaxially grown we cannot use lift-off either. Within these constraints, an appropriate fabrication recipe for low loss Ge waveguide must be developed.

8.3. Photo Thermal Spectroscopy (PTS)

The sensors we introduced in chapter 5 record optical intensity changes due to absorption of a chemical vapor. However, the peak absorption cross-section of most vapors are about 10-18 cm2/molecule (e.g. for methane, at =3.3 μm, the cross-section is about 1.6×10-18 cm2/molecule). At room temperature and 1 atm pressure, the intensity change recorded is less than 0.001 %, when 1 ppm methane gas interacts with light over a 1 cm waveguide length. By integration with both light source and detector, we can eliminate the vibrational noise caused by misalignment, improve the coupled power and thus increase the sensitivity. Ebeam lithography also provides better sidewall roughness and can decrease the scattering loss of waveguide, which enables longer device within the energy budget. All these improvements can push the detection limit to ppm level. Other than those improvements on current design, to reach ppm or ppb level detection on-chip, different physical principles can be leveraged.

Photo Thermal Spectroscopy (PTS) provides a highly sensitive and precise method for measuring infrared molecules[108]. The temperature of a resonator increases when a strong pump light is critically coupled into it. A small portion of the light through the resonator will be absorbed by approaching gas molecules, cooling the resonator and moving it away from thermal equilibrium. This cooling shifts the resonant peak, and can

be detected by another low-energy probe light. This couples the thermo-optic effect with the absorption of chemicals. The sensitivity of the device based on this mechanism can provide an enhancement factor up to ~2000 with respect to the traditional transmission IR spectroscopy technology[109,110].

For normal PTS devices, a laser power of about 100 mW is needed to heat the device. To pump a high-Q resonator the laser source has to be finely tunable, typically requiring an external cavity. Both are challenges for an integrated light source with limited on-chip power and thermal budget.

8.4. Polymer-assisted sensing

Another way to increase the sensitivity of our sensor is to use special chemicals (usually polymer coatings) to concentrate the target vapor. This will increase sensitivity and selectivity. For example, xylene can be concentrated into PDMS with a partition coefficient of about 1000 [111]. Xylene vapor can be captured or released depending on the environmental xylene concentration, making the PDMS-coated device a much more sensitive reversible sensor. Selectivity of a sensor improves when targeting bio-molecules using special enzymes or functional groups[112,113]. For irreversible applications, a nano-foam coating can also improve the sensitivity and selectivity of our sensor[100].

8.5. Phase change materials in photonics

Phase change materials are not new to photonics. Since the first rewritable optical disc was made in 1999, chalcogenide glass based phase change materials have been used. The traditional GeSbTe material is stable, but requires high energy to effect a phase transition besides being slow. Different phase change materials can be introduced.

On July 2015, Intel Corp. and Micron Tech. Inc. announced their new nonvolatile memory called "XPoint" which is based on phase change materials. The transition speed was claimed to be 1,000 times higher than flash memory and although the ingredient was company confidential, based on patent searches it is likely a chalcogenide material. Fast switches, optical routers and modulators can now be envisioned.

8.6. Thermal isolation and cooling on the chip

As mentioned in chapter 7, we cooled the PbTe thin film (non-integrated sample) to get a better signal to noise ratio when using our (moderately strong) MIR broadband light source. Decreasing dark current with cooling decreases the noise level and power consumption.

At lower temperature, the intrinsic carrier concentration of PbTe drops, resulting in higher resistance and lower dark current. The change of the resistance of sample 1 in Chapter 7 is shown in Figure 8-3. If follows an exponential relationship with the inverse of the temperature:

$$R \propto \frac{1}{n_i} \propto \exp(\frac{E_g}{2k_B T})$$

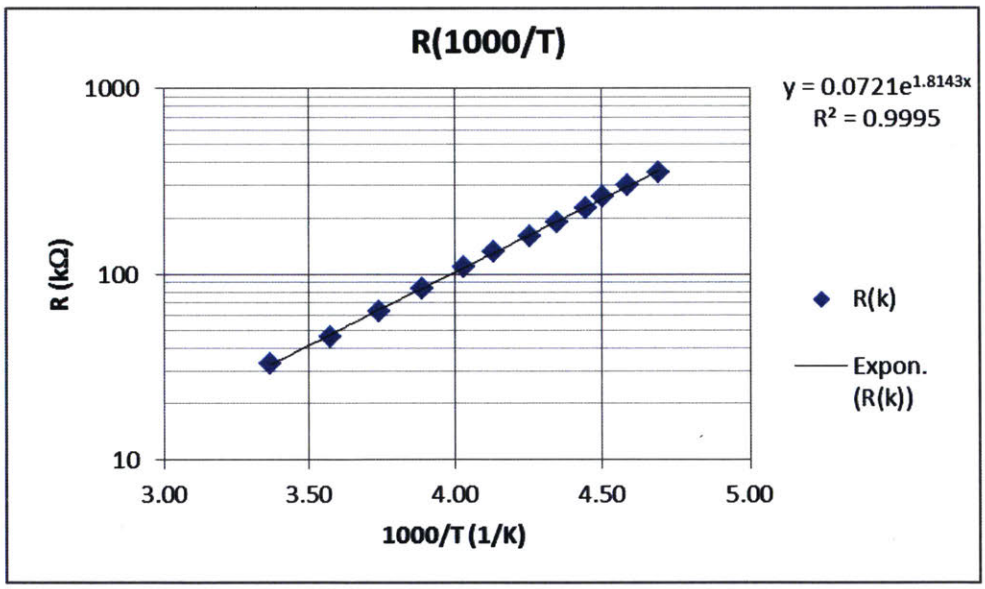

Figure 8-3 Resistance change with temperature for 650 nm thick PbTe thin film.

For an integrated device, cooling strategies must be developed to avoid the following major issues.

1) Moisture condensation

When cooled down below 0 °C, moisture in the ambient air will condense on the

sample surface, compromising sample and data integrity by modifying its temperature and resistance. To prevent this, a non-integrated sample can be sealed in a MIR-transparent glass chamber. This sealing is not possible for an integrated sample, because the coupling distance between lens and the waveguide is too close (less than 100 μm) and it is hard to build such thin chamber walls.

An alternative is to constantly flow low temperature nitrogen gas (e.g. from liquid nitrogen cylinder) over the sample to get rid of the moisture. However, the vibration due to the air flow can affect optical alignment, thus increasing noise level, besides being a showstopper for a mobile application.

We can also coat the sample with transparent protection layers (such as photoresist SU-8 for 1550 nm) to avoid damage from condensation as long as the light propagation is not affected by the coating. However, the condensation will still occur in the exposed regions of the sample.

2) Thermal isolation

When integrated with other electrical or optical components, not all of them work properly under low temperature. If we can thermally isolate only the detector, we can decrease the cooling power requirement while keeping other components at room temperature.

The silicon oxide and the silicon substrate have relatively high thermal conductivity, which is ideal to transfer heat from the detector to the TEC cooler at the back of the wafer. But it is not ideal to isolate the PbTe detector from other components.

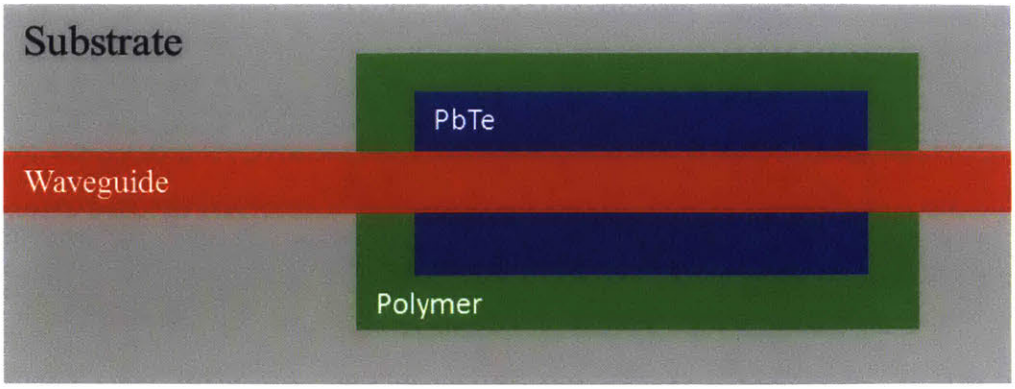

Figure 8-4 Top-view schematic of the thermal isolation design for PbTe detector. A trench is etched and low thermal conductivity polymer is used to fill the trench.

One possible way is to etch a trench around the PbTe region and suspend the waveguides connected to the detector. But if the leftover substrate is not thin enough, there will still be heat transfer from the substrate. As shown in Figure 8-4, a possible solution is to etch through the silicon wafer and fill the slot with low-thermal-conductivity polymers, which maintains the mechanical strength while serving as a thermal shield.

In conclusion, by improving in all the sections described above, we can shrink the current large MIR spectrum analysis equipment to a chip-size device. The cost and the energy consumption of the tools will decrease. Integration with other CMOS technology, including computing, remote communication, power management, etc. makes the sensing smart.

References

(1) Hodgkinson, J.; Tatam, R. P. *Measurement Science and Technology* **2013**, *24*, 012004.

(2) Singh, V.; Lin, P. T.; Patel, N.; Lin, H.; Li, L.; Zou, Y.; Deng, F.; Ni, C.; Hu, J.; Giammarco, J. *Science and Technology of Advanced Materials* **2014**, *15*, 014603.

(3) Yang, R. Q.; Yang, B.; Zhang, D.; Lin, C.-H.; Murry, S.; Wu, H.; Pei, S. *Applied physics letters* **1997**, *71*, 2409.

(4) Kim, M.; Canedy, C.; Bewley, W.; Kim, C.; Lindle, J.; Abell, J.; Vurgaftman, I.; Meyer, J. *Applied Physics Letters* **2008**, *92*, 1110.

(5) Faist, J.; Capasso, F.; Sivco, D. L.; Sirtori, C.; Hutchinson, A. L.; Cho, A. Y. *Science* **1994**, *264*, 553.

(6) Meyer, J.; Vurgaftman, I.; Yang, R.; Ram-Mohan, L. *Electronics Letters* **1996**, *32*, 45.

(7) Giammarco, J.; Zdyrko, B.; Petit, L.; Musgraves, J. D.; Hu, J.; Agarwal, A.; Kimerling, L.; Richardson, K.; Luzinov, I. *Chemical Communications* **2011**, *47*, 9104.

(8) Rogalski, A. *Progress in quantum electronics* **2003**, *27*, 59.

(9) Fang, A. W.; Park, H.; Cohen, O.; Jones, R.; Paniccia, M. J.; Bowers, J. E. *Optics Express* **2006**, *14*, 9203.

(10) Wu, M. C.; Solgaard, O.; Ford, J. E. *Lightwave Technology, Journal of* **2006**, *24*, 4433.

(11) Liu, J.; Sun, X.; Camacho-Aguilera, R.; Kimerling, L. C.; Michel, J. *Optics letters* **2010**, *35*, 679.

(12) Liu, J.; Cannon, D. D.; Ishikawa, Y.; Wada, K.; Danielson, D. T.; Jongthammanurak, S.; Michel, J.; Kimerling, L. C. *Phys. Rev. B* **2004**, *70*, 155309.

(13) Xiaoxin Wang, R. C.-A., Yan Cai, Lionel C Kimerling, Jurgen Michel and Jifeng Liu *Optics Letters* **2012**.

(14) Chuang, S. L. *Physics of optoelectronic devices (Series in pure & applied optics)*; New York: Wiley, 2009.

(15) Sun, X.; Liu, J.; Kimerling, L. C.; Michel, J. **2009**.

(16) Fischetti, M.; Laux, S. *Journal of Applied Physics* **1996**, *80*, 2234.

(17) Jain, J. R.; Hryciw, A.; Baer, T. M.; Miller, D. A.; Brongersma, M. L.; Howe, R. T. *Nature Photonics* **2012**, *6*, 398.

(18) Ghrib, A.; De Kersauson, M.; El Kurdi, M.; Jakomin, R.; Beaudoin, G.; Sauvage, S.; Fishman, G.; Ndong, G.; Chaigneau, M.; Ossikovski, R. *Applied Physics Letters* **2012**, *100*, 201104.

(19) Ye, C.; Hewak, D.; Hempstead, M.; Samson, B.; Payne, D. *Journal of non-crystalline solids* **1996**, *208*, 56.

(20) Arguirov, T.; Kittler, M.; Abrosimov, N. In *Journal of Physics: Conference Series*; IOP Publishing: 2011; Vol. 281, p 012021.

(21) El Kurdi, M.; Fishman, G.; Sauvage, S.; Boucaud, P. *Journal of Applied Physics* **2010**, *107*, 013710.

(22) Van Driel, H.; Elci, A.; Bessey, J.; Scully, M. O. *Solid State Communications* **1976**, *20*, 837.

(23) Sommers Jr, H. *Physical Review* **1961**, *124*, 1101.
(24) Berggren, K. F.; Sernelius, B. E. *Physical Review B* **1981**, *24*, 1971.
(25) Jain, S.; Roulston, D. *Solid-state electronics* **1991**, *34*, 453.
(26) Haas, C. *Physical Review* **1962**, *125*, 1965.
(27) Rodolfo Camacho-Aguilera, Z. H., Yan Cai, Lionel C. Kimerling, Jurgen Michel **2012**.
(28) Kalt, H.; Rinker, M. *Physical Review B* **1992**, *45*, 1139.
(29) Haas, C. *Physical Review* **1962**, *125*, 1965.
(30) Pankove, J.; Aigrain, P. *Physical Review* **1962**, *126*, 956.
(31) Karpova, I.; Perel, V.; Syrovegin, S. *Soviet Physics Semiconductors-Ussr* **1989**, *23*, 518.
(32) Cai, Y.; Han, Z.; Wang, X.; Camacho-Aguilera, R. E.; Kimerling, L. C.; Michel, J.; Liu, J. *Selected Topics in Quantum Electronics, IEEE Journal of* **2013**, *19*, 1901009.
(33) Katsaros, G.; Stoffel, M.; Rastelli, A.; Schmidt, O. G.; Kern, K.; Tersoff, J. *Appl. Phys. Lett.* **2007**, *91*.
(34) Ratto, F.; Rosei, F.; Locatelli, A.; Cherifi, S.; Fontana, S.; Heun, S.; Szkutnik, P. D.; Sgarlata, A.; De Crescenzi, M.; Motta, N. *J. Appl. Phys.* **2005**, *97*.
(35) Froyen, S.; Wood, D. M.; Zunger, A. *Thin Solid Films* **1989**, *183*, 33.
(36) Peng, C. S.; Huang, Q.; Cheng, W. Q.; Zhou, J. M.; Zhang, Y. H.; Sheng, T. T.; Tung, C. H. *Physical Review B* **1998**, *57*, 8805.
(37) Wang, K. L.; Cha, D.; Liu, J.; Chen, C. *Proceedings of the Ieee* **2007**, *95*, 1866.
(38) Giorgioni, A.; Gatti, E.; Grilli, E.; Chernikov, A.; Chatterjee, S.; Chrastina, D.; Isella, G.; Guzzi, M. *J. Appl. Phys.* **2012**, *111*.
(39) Niquet, Y. M.; Allan, G.; Delerue, C.; Lannoo, M. *Appl. Phys. Lett.* **2000**, *77*, 1182.
(40) Takeoka, S.; Fujii, M.; Hayashi, S.; Yamamoto, K. *Physical Review B* **1998**, *58*, 7921.
(41) Shin-ichi Saito, K. O., Kazuki Tania, Makoto Takahashi, Etsuko Nomoto, Tadashi Okumura, Yuji Suwa, Yong Lee, Misuzu Sagawa, Toshiki Sugawara and Tatemi Ido *ECS Transaction* **2012**, *45*, 103.
(42) Yao, Y.; Hoffman, A. J.; Gmachl, C. F. *Nature Photonics* **2012**, *6*, 432.
(43) Schweizer, T.; Brady, D.; Hewak, D. W. *Optics Express* **1997**, *1*, 102.
(44) Többen, H. *Electronics Letters* **1992**, *28*, 1361.
(45) Wetenkamp, L.; Westendorf, T.; West, G.; Kober, A. In *Materials Science Forum*; Trans Tech Publ: 1991; Vol. 32, p 471.
(46) Al Tal, F.; Dimas, C.; Hu, J.; Agarwal, A.; Kimerling, L. C. *Optics Express* **2011**, *19*, 11951.
(47) Han, Z.; Zhang, L.; Kimerling, L. C.; Agarwal, A. M. *Selected Topics in Quantum Electronics, IEEE Journal of* **2015**, *21*, 311.
(48) Brady, D.; Schweizer, T.; Wang, J.; Hewak, D. *Journal of non-crystalline solids* **1998**, *242*, 92.
(49) Zhang, L.; Yang, C.-X. *Chinese Physics Letters* **2004**, *21*, 1542.

(50) Bao, C.; Zhang, L.; Matsko, A.; Yan, Y.; Zhao, Z.; Xie, G.; Agarwal, A. M.; Kimerling, L. C.; Michel, J.; Maleki, L. *Optics letters* **2014**, *39*, 6126.

(51) Zhang, L.; Mu, J.; Singh, V.; Agarwal, A. M.; Kimerling, L. C.; Michel, J. *Selected Topics in Quantum Electronics, IEEE Journal of* **2014**, *20*, 111.

(52) Zhang, L.; Lin, Q.; Yue, Y.; Yan, Y.; Beausoleil, R. G.; Willner, A. E. *Optics express* **2012**, *20*, 1685.

(53) Luke, K.; Dutt, A.; Poitras, C. B.; Lipson, M. *Optics express* **2013**, *21*, 22829.

(54) Nam, K. H.; Park, I. H.; Ko, S. H. *Nature* **2012**, *485*, 221.

(55) Martin, P. A. *Chemical Society Reviews* **2002**, *31*, 201.

(56) Schneider, R. C.; Kovar, K.-A. *Forensic science international* **2003**, *134*, 187.

(57) Hocde, S.; Lore, O.; Sire, O.; Boussard-Ple, C.; Bureau, B.; Turlin, B.; Keirsse, J.; Leroyer, P.; Lucas, J. *Journal of biomedical optics* **2004**, *9*, 404.

(58) Ma, P.; Choi, D.-Y.; Yu, Y.; Gai, X.; Yang, Z.; Debbarma, S.; Madden, S.; Luther-Davies, B. *Optics express* **2013**, *21*, 29927.

(59) Luff, B.; Wilkinson, J. S.; Piehler, J.; Hollenbach, U.; Ingenhoff, J.; Fabricius, N. *Journal of lightwave technology* **1998**, *16*, 583.

(60) Hua, P.; Luff, B. J.; Quigley, G. R.; Wilkinson, J. S.; Kawaguchi, K. *Sensors and Actuators B: Chemical* **2002**, *87*, 250.

(61) Fadel, L.; Lochon, F.; Dufour, I.; Francais, O. *Journal of Micromechanics and Microengineering* **2004**, *14*, S23.

(62) Robinson, J. T.; Chen, L.; Lipson, M. *Optics express* **2008**, *16*, 4296.

(63) Lai, W.-C.; Chakravarty, S.; Wang, X.; Lin, C.; Chen, R. T. *Optics letters* **2011**, *36*, 984.

(64) Anne, M.-L.; Keirsse, J.; Nazabal, V.; Hyodo, K.; Inoue, S.; Boussard-Pledel, C.; Lhermite, H.; Charrier, J.; Yanakata, K.; Loreal, O. *Sensors* **2009**, *9*, 7398.

(65) Smith, C. J.; Shankar, R.; Laderer, M.; Frish, M. B.; Loncar, M.; Allen, M. G. *Optics express* **2015**, *23*, 5491.

(66) Chen, Y.; Lin, H.; Hu, J.; Li, M. *ACS nano* **2014**, *8*, 6955.

(67) Lin, P. T.; Singh, V.; Wang, J.; Lin, H.; Hu, J.; Richardson, K.; Musgraves, J. D.; Luzinov, I.; Hensley, J.; Kimerling, L. C. *Optical Materials Express* **2013**, *3*, 1474.

(68) Wang, X.; Antoszewski, J.; Putrino, G.; Lei, W.; Faraone, L.; Mizaikoff, B. *Analytical chemistry* **2013**, *85*, 10648.

(69) Sieger, M.; Balluff, F.; Wang, X.; Kim, S.-S.; Leidner, L.; Gauglitz, G.; Mizaikoff, B. *Analytical chemistry* **2012**, *85*, 3050.

(70) Roelkens, G.; Dave, U.; Gassenq, A.; Hattasan, N.; Hu, C.; Kuyken, B.; Leo, F.; Malik, A.; Muneeb, M.; Ryckeboer, E. *Optical Materials Express* **2013**, *3*, 1523.

(71) Zou, Y.; Wray, P.; Chakravarty, S.; Chen, R. T. In *CLEO: Applications and Technology*; Optical Society of America: 2015, p AF2J. 1.

(72) Richardson, K.; Petit, L.; Carlie, N.; Zdyrko, B.; Luzinov, I.; Hu, J.; Agarwal, A.; Kimerling, L.; Anderson, T.; Richardson, M. *Journal of Nonlinear Optical Physics & Materials* **2010**, *19*, 75.

(73) Böberl, M.; Fromherz, T.; Roither, J.; Pillwein, G.; Springholz, G.; Heiss, W. *Applied physics letters* **2006**, *88*, 1105.

(74) Kimerling, L.; Dal Negro, L.; Saini, S.; Yi, Y.; Ahn, D.; Akiyama, S.; Cannon, D.; Liu, J.; Sandland, J.; Sparacin, D.; Springer, ISBN: 2004.

(75) Pernice, W. H.; Bhaskaran, H. *Applied Physics Letters* **2012**, *101*, 171101.

(76) Ikuma, Y.; Saiki, T.; Tsuda, H. *IEICE Electronics Express* **2008**, *5*, 442.

(77) Ikuma, Y.; Shoji, Y.; Kuwahara, M.; Wang, X.; Kintaka, K.; Kawashima, H.; Tanaka, D.; Tsuda, H. *Electronics Letters* **2010**, *46*, 1460.

(78) Lankhorst, M. H.; Ketelaars, B. W.; Wolters, R. *Nature materials* **2005**, *4*, 347.

(79) Wang, W.; Shi, L.; Zhao, R.; Lim, K.; Lee, H.; Chong, T.; Wu, Y. *Applied Physics Letters* **2008**, *93*, 043121.

(80) Zhang, T.; Song, Z.; Gong, Y.; Lin, Y.; Xu, C.; Chen, Y.; Liu, B.; Feng, S. *Applied Physics Letters* **2008**, *92*, 3503.

(81) Kang, D.-H.; Kim, I. H.; Jeong, J.-h.; Cheong, B.-k.; Ahn, D.-H.; Lee, D.; Kim, H.-M.; Kim, K.-B.; Kim, S.-H. *Journal of Applied Physics* **2006**, *100*, 054506.

(82) Giraud, V.; Cluzel, J.; Sousa, V.; Jacquot, A.; Dauscher, A.; Lenoir, B.; Scherrer, H.; Romer, S. *Journal of Applied Physics* **2005**, *98*, 013520.

(83) Serway, R. A.; Jewett, J. W. *Principles of physics*; Saunders College Pub. Fort Worth, TX, 1998; Vol. 1.

(84) Huang, D.; Miao, X.; Li, Z.; Sheng, J.; Sun, J.; Peng, J.; Wang, J.; Chen, Y.; Long, X. *Applied Physics Letters* **2011**, *98*, 242106.

(85) Rogalski, A. *Opto-Electronics Review* **2012**, *20*, 279.

(86) Soref, R. *Nature Photonics* **2010**, *4*, 495.

(87) Werle, P.; Slemr, F.; Maurer, K.; Kormann, R.; Mücke, R.; Jänker, B. *Optics and lasers in engineering* **2002**, *37*, 101.

(88) Ahn, D.; Hong, C.-y.; Liu, J.; Giziewicz, W.; Beals, M.; Kimerling, L. C.; Michel, J.; Chen, J.; Kärtner, F. X. *Optics Express* **2007**, *15*, 3916.

(89) Fang, A. W.; Jones, R.; Park, H.; Cohen, O.; Raday, O.; Paniccia, M. J.; Bowers, J. E. *Optics express* **2007**, *15*, 2315.

(90) Han, Z.; Lin, P.; Singh, V.; Kimerling, L.; Hu, J.; Richardson, K.; Agarwal, A.; Tan, D. *Applied Physics Letters* **2016**, *108*, 141106.

(91) Hattasan, N.; Gassenq, A.; Cerutti, L.; Rodriguez, J.-B.; Tournié, E.; Roelkens, G. *IEEE Photonics Technology Letters* **2011**, *23*, 1760.

(92) Gassenq, A.; Hattasan, N.; Cerutti, L.; Rodriguez, J. B.; Tournié, E.; Roelkens, G. *Optics express* **2012**, *20*, 11665.

(93) Margarit, J. M.; Vergara, G.; Villamayor, V.; Gutierrez-Alvarez, R.; Fernandez-Montojo, C.; Teres, L.; Serra-Graells, F. *Solid-State Circuits, IEEE Journal of* **2015**, *50*, 2394.

(94) Komissarova, T.; Khokhlov, D.; Ryabova, L.; Dashevsky, Z.; Kasiyan, V. *Physical Review B* **2007**, *75*, 195326.

(95) Wang, J.; Zens, T.; Hu, J.; Becla, P.; Kimerling, L. C.; Agarwal, A. M. *Applied Physics Letters* **2012**, *100*, 211106.

(96) Wang, J.; Hu, J.; Becla, P.; Agarwal, A. M.; Kimerling, L. C. *Optics express* **2010**, *18*, 12890.

(97) Wang, J.; Hu, J.; Becla, P.; Agarwal, A. M.; Kimerling, L. C. *Journal of Applied Physics* **2011**, *110*, 083719.

(98) Wang, J.; Hu, J.; Sun, X.; Agarwal, A. M.; Kimerling, L. C.; Lim, D. R.; Synowicki, R. *Journal of applied physics* **2008**, *104*, 053707.

(99) Hu, J.; Tarasov, V.; Agarwal, A.; Kimerling, L.; Carlie, N.; Petit, L.; Richardson, K. *Optics Express* **2007**, *15*, 2307.

(100) Singh, V.; Zens, T.; Hu, J.; Wang, J.; Musgraves, J. D.; Richardson, K.; Kimerling, L. C.; Agarwal, A. *Sensors and Actuators B: Chemical* **2013**, *185*, 195.

(101) Boreman, G. D. *Infrared detectors and systems*; Wiley-Interscience, 1996; Vol. 24.

(102) Melngailis, I.; Harman, T. *Applied Physics Letters* **1968**, *13*, 180.

(103) Adam, J. L.; Calvez, L.; Trolès, J.; Nazabal, V. *International Journal of Applied Glass Science* **2015**, *6*, 287.

(104) Stegeman, R.; Stegeman, G.; Delfyett, P.; Petit, L.; Carlie, N.; Richardson, K.; Couzi, M. *Optics Express* **2006**, *14*, 11702.

(105) Lindblom, M.; Reinspach, J.; von Hofsten, O.; Bertilson, M.; Hertz, H. M.; Holmberg, A. *Journal of Vacuum Science & Technology B* **2009**, *27*, L1.

(106) Oehrlein, G.; Bestwick, T.; Jones, P.; Jaso, M.; Lindström, J. *Journal of The Electrochemical Society* **1991**, *138*, 1443.

(107) Campo, A.; Cardinaud, C.; Turban, G. *Journal of Vacuum Science & Technology B* **1995**, *13*, 235.

(108) Hu, J. *Optics Express* **2010**, *18*, 22174.

(109) Davis, C. C.; Petuchowski, S. J. *Applied optics* **1981**, *20*, 2539.

(110) Dovichi, N. J.; Harris, J. *Analytical chemistry* **1979**, *51*, 728.

(111) Zou, Y.; Subbaraman, H.; Chakravarty, S.; Xu, X.; Hosseini, A.; Lai, W.-C.; Chen, R. T. In *SPIE OPTO*; International Society for Optics and Photonics: 2014, p 89900X.

(112) Gabl, R.; Feucht, H.-D.; Zeininger, H.; Eckstein, G.; Schreiter, M.; Primig, R.; Pitzer, D.; Wersing, W. *Biosensors and Bioelectronics* **2004**, *19*, 615.

(113) Ksendzov, A.; Lin, Y. *Optics letters* **2005**, *30*, 3344.